ACS APPLIED MATERIALS & INTERFACES

Research Article

www.acsami.org

Composition-Dependent Morphostructural Properties of Ni–Cu Oxide Nanoparticles Confined within the Channels of Ordered Mesoporous SBA-15 Silica

Adrian Ungureanu,*[,†] Brindusa Dragoi,[†] Alexandru Chirieac,[†] Carmen Ciotonea,[†] Sébastien Royer,*[,‡] Daniel Duprez,[‡] Anne Sophie Mamede,[§] and Emil Dumitriu[†]

[†]Faculty of Chemical Engineering and Environmental Protection, "Gheorghe Asachi" Technical University of Iasi, 73 Prof. D. Mangeron Boulevard, 700050 Iasi, Romania

[‡]Université de Poitiers, CNRS UMR 7285, IC2MP, 4 Rue Michel Brunet, 86022 Poitiers Cedex, France

[§]Université de Lille 1, UCCS UMR 8181 CNRS, Bât C3, 59650 Villeneuve d'Ascq Cedex, France

Supporting Information

ABSTRACT: NiO and NiO–CuO polycrystalline rodlike nanoparticles were confined and stabilized within the channels of ordered mesoporous SBA-15 silica by a simple and viable approach consisting in incipient wetness impregnation of the calcined support with aqueous solutions of metal nitrates followed by a mild drying step at 25 °C and calcination. As revealed by low- and high-angle XRD, N_2 adsorption/desorption, HRTEM/EDXS and H_2 TPR analyses, the morphostructural properties of NiO–CuO nanoparticles can be controlled by adjusting their chemical composition, creating the prerequisites to obtain high performance bimetallic catalysts. Experimental evidence by in situ XRD monitoring during the thermoprogrammed reduction indicates that the confined NiO–CuO nanoparticles evolve into thermostable and well-dispersed Ni–Cu heterostructures. The strong Cu–Ni and Ni–support interactions demonstrated by TPR and XPS were put forward to explain the formation of these new bimetallic structures. The optimal Ni–Cu/SBA-15 catalyst (i.e., Cu/(Cu+Ni) atomic ratio of 0.2) proved a greatly enhanced reducibility and H_2 chemisorption capacity, and an improved activity in the hydrogenation of cinnamaldehyde, as compared with the monometallic Ni/SBA-15 or Cu/SBA-15 counterparts, which can be associated with the synergism between nickel and copper and high dispersion of active components on the SBA-15 host. The unique structure and controllable properties of both oxidic and metallic forms of Ni–Cu/SBA-15 materials make them very attractive for both fundamental research and practical catalytic applications.

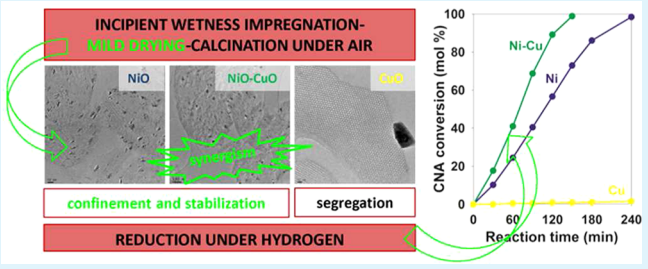

KEYWORDS: *mesoporous materials, SBA-15, impregnation, bimetallic nanoparticles, confinement, hydrogenation*

1. INTRODUCTION

In the field of heterogeneous catalysis, highly dispersed supported (bi)metallic (oxide) nanoparticles (NPs) have received much attention in recent years because of their high activity and/or selectivity in important oxidation and (de)-hydrogenation reactions underpinning most of the catalytic applications in environmental pollution control, energy, and fine chemistry.[1,2] It was accepted that the unique catalytic properties of the supported NPs are directly related to their morphostructure (i.e., size and shape), metal (oxide) dispersion (i.e., surface-to-volume ratio and the number of defect sites, kinks, steps, edges, and corners), concentration and the electronic properties of the metals within their host environment.[3,4] However, the low stability of NPs during the high-temperature catalyst activation (e.g., air calcination, hydrogen reduction) or high-temperature catalytic reactions (e.g., hydrocarbon steam reforming) largely limits their application because it results in particle sintering and restructuring, and loss of dispersion and catalytic activity.[5,6] In some instances, metal NPs can be encapsulated or even detached from the support by formation of carbon filaments, which dramatically decreases the catalyst lifetime.[7] Therefore, the design and development of specific supported metal (oxide) nanoparticles with a high and thermally stable dispersion represent ongoing and challenging research tasks.

The discovery of ordered mesoporous materials (e.g., MCM-41, SBA-15)[8,9] provided enormous opportunities to address this challenge because their unique pore architecture make them very attractive as hosts for the confinement and stabilization of uniform NPs,[10−12] which can better maintain their dispersion and catalytic performance even under high-temperature conditions.[13] Particularly, ordered mesoporous

Received: November 16, 2012
Accepted: March 15, 2013
Published: March 15, 2013

SBA-15 materials present a series of characteristics which recommend them as ideal host structures: (i) an improved framework cross-linking and thick walls (3−6 nm), and high (hydro)thermal stability,[14] (ii) large specific surface areas (600−1000 m^2 g^{-1}), allowing a high dispersion and increased concentration of active sites, and more importantly, (iii) well-defined dual pore structures composed of hexagonal arrays of large and tunable primary cylindrical mesopores (i.e., diameters of 5−10 nm) as well as secondary (ultra)supermicropores and/or small mesopores,[15] allowing the confinement of NPs in one pore system or both, and enhancing the control over their morphology, location and stability.[16−19] Therefore, much effort was made to prepare metal (oxide) NPs confined in the pores of SBA-15 and to investigate their morphostructural and/or catalytic properties.[19−26] As awaited, the results demonstrated that the special microenvironment of SBA-15 nanopores significantly inhibits the growth of NPs, resulting in interesting properties and functions required for applications in catalysis, such as enhanced thermostability[19,21] and superior catalytic activity.[23,24] For example, Ag NPs confined in the mesopores of SBA-15 demonstrated improved resistance to sintering as compared with unconfined Ag NPs (i.e., supported on conventional silica) even at temperatures higher than the corresponding Tammann temperature.[21] Pd−Au alloy NPs confined within the channels of mesoporous silica were found recently to be highly active in the hydrogenation of cinnamaldehyde.[24] Nevertheless, the successful synthetic routes for the inclusion of NPs within the channels of SBA-15 are nowadays highly sophisticated and therefore difficult to scale-up (e.g., in situ encapsulation of nanoclusters, organometallic methodologies, and surface functionalization schemes with/or without in situ reduction),[13] and in many cases, they still lack the control over the thermal stability of nanoparticles.[21,22] For instance, when a high-temperature step is involved (e.g., thermolysis of grafted organic ligand anchoring the metal cations to get (oxide) metal NPs), the metal−support interaction decreases and the initially stabilized particles easily diffuse out of mesopores and form large agglomerates.[22] Likewise, most of the preparation protocols were optimized to obtain catalysts based on expensive and scarce noble metals such as Pt,[20] Pd,[19,24] Au,[22,23] or Ag,[21] yet the resource economy status quo would rather promote the development of cost-effective catalysts based on non-noble metal components.[18,25,26]

Within this context, the incipient wetness impregnation (IWI) using aqueous solutions of metal nitrates came back into focus as an attractive route for encapsulating non-noble metal (oxide) NPs (e.g., Ni-, Cu-, and Co-based) within the mesopores of SBA-15,[6,27] owing to some inherent sustainability-related advantages such as convenience, low amount of required solvent, availability and low cost of metal sources, high purity of metal precursor phases and limited production of waste. Nonetheless, in a series of landmark papers on the IWI method, de Jong et al.[5,6,27,28] have reported that without special calcination conditions (e.g., gas flow of NO/Ar instead of stagnant air), it is difficult to control the dispersion and thermal stability of metal (oxide) NPs. This is due to the weak metal precursor-support interactions which result in the transport of oxidic precursor phases outside the SBA-15 nanopores and location on the external surface as large aggregates. Therefore, new convenient IWI routes to confine and stabilize metal (oxide) NPs in the channels of SBA-15 are still being sought after. We have previously reported that the gentle drying of the metal precursor/silica composites (i.e., at room temperature) after the initial incipient wetness impregnation step creates favorable conditions to prevent the transport of metal precursors at the external surface during calcination under stagnant air.[29] The viability of this simple approach (referred thereafter as IWI-MD; MD stands for mild drying) was shown for the Ni−Cu/SBA-15 materials that display high thermal stability, both during air calcination and hydrogen reduction, respectively. It was preliminary proposed that the NiO−CuO NPs are stabilized by a confinement effect of the micro/mesoporous structure of SBA-15 and by strong Ni−Cu and Ni−silica interactions, yet in-depth investigations are compulsory to shed more light. From a broader and practical perspective, the scientific interest in supported bimetallic Ni−Cu NPs also arises because of their enhanced catalytic activity and/or selectivity relative to single-component catalysts, as shown in a wide variety of chemical reactions such as hydrocarbon steam reforming,[30,31] NO_x reduction,[32] CO hydrogenation,[33] methane partial oxidation,[34,35] water gas shift,[36] glycerol hydrogenolysis,[37] hydrogenation of aromatics,[38] as well as chemoselective hydrogenation of α,β-unsaturated aldehydes.[39−41] The catalytic properties of bimetallic Ni−Cu NPs were usually associated with the synergistic effects between Ni and Cu atoms (i.e., geometric and/or electronic effects), as already proposed in the early literature.[42,43]

This contribution aims to further investigate the effect of chemical composition on the specific morphostructural properties of NiO−CuO nanoparticles confined and stabilized within the channels of ordered SBA-15 silica by IWI-MD approach. To this end, a set of nickel and copper-containing samples were prepared by progressively substituting Ni with Cu and systematically characterized and compared with the corresponding single-component materials. The oxide forms of catalysts were first analyzed for their bulk chemical composition, structure, texture, particle morphology and microstructure, as well as reducibility and surface chemical composition. The crystal phase evolution of NiO−CuO nanoparticles during the thermoprogrammed reduction process was monitored by in situ X-ray Diffraction to further explore the structure and thermostability of evolved bimetallic nanoparticles. The metal forms of catalysts were then analyzed by XPS and hydrogen chemisorption in order to probe the surface composition of bimetallic Ni−Cu nanoparticles. The catalytic effectiveness of the Ni−Cu/SBA-15 materials was finally illustrated in the chemoselective hydrogenation of cinnamaldehyde as a benchmark reaction which is highly sensitive to the properties of supported bimetallic nanoparticles (e.g., nature of metals and d-bandwidth, nature of support, particle morphology, surface chemical composition, in relation to the catalyst preparation method and pretreatment conditions).[44,45]

2. EXPERIMENTAL SECTION

2.1. Materials. All chemicals required to prepare the mesoporous SBA-15 silica and the catalysts were used as purchased: tetraethylorthosilicate ($Si(OC_2H_5)_4$, TEOS, 98%, Sigma-Aldrich), nonionic triblock copolymer Pluronic P123 (poly(ethyleneoxide)-block-poly(propyleneoxide)-block-poly(ethyleneoxide)-block), $EO_{20}PO_{70}EO_{20}$, molecular weight of 5800, BASF Corp.), hydrochloric acid (HCl, 37%, Sigma-Aldrich), nickel nitrate ($Ni(NO_3)_2{\cdot}6H_2O$, 98%, Sigma-Aldrich) and copper nitrate ($Cu(NO_3)_2{\cdot}3H_2O$, 98%, Sigma-Aldrich). For the catalytic runs, the chemicals were also used as purchased: trans-cinnamaldehyde ($C_6H_5CH{=}CHCHO$, 98%, Merck) as reagent and propylene carbonate ($C_4H_6O_3$, 99%, Sigma-Aldrich) as solvent.

2.2. Preparation of Samples. A single batch synthesis of pure silica SBA-15 (~ 7.5 g) with homogeneous grain morphology and size (see the Supporting Information, Figure S1) was carried out following the classical literature protocol.[9] Twelve grams of Pluronic P123 and 450 mL of 1.6 M HC1 aqueous solution were stirred at 40 °C until the complete dissolution of the polymer. The appropriate amount of TEOS (25.5 g) was then added dropwise to the polymer solution, followed by magnetic stirring for 24 h. The resulting gel was transferred into a 1000 mL polypropylene bottle and heated at 100 °C for 48 h. The final solid was recovered by filtration, washed with demineralized water and dried at 80 °C overnight. The open pore structures were obtained by calcination of the as-synthesized SBA-15 materials (~1.2 g at once) under stagnant air in a muffle oven at 550 °C for 6 h (heating ramp of 1.5 °C min^{-1}). The freshly calcined SBA-15 solids were stored in a desiccator at room temperature for at least 2 days up to their use as supports.

Metal oxide-loaded SBA-15 samples were prepared by incipient wetness impregnation of micro/mesoporous SBA-15 support (total pore volume of 1.12 cm^3 g^{-1}, vide infra) with the corresponding aqueous metal nitrate precursor solutions to obtain a constant loading of zerovalent metal components of 6 wt % and variable Cu/M atomic ratio (in the range 0−1; M = Cu+Ni). The metal precursor/silica composites were gently dried under air at 25 ± 1 °C for 48 h. The powders were sequentially submitted to calcination under stagnant air in a muffle oven having a smog exit (Vulcan A-550; chamber dimensions (width × height × depth): 23.6 × 18.0 × 22.5 cm) at 500 °C for 6 h (heating ramp of 1.5 °C min^{-1}) to obtain the oxide forms of catalysts. To avoid the "container effect" during calcination,[46] the same open crucibles and similar sample depths were used. After calcination, the solids were stored under ambient conditions in sealed containers without special precautions. The monocomponent and bicomponent samples were labeled according to their chemical composition as NC_w, where N and C stand for Ni and Cu, respectively, and *w* stands for the Cu/M ratio (M = Cu+Ni).

For comparative purposes, a nickel oxide-loaded SBA-15 sample (6 wt %) was prepared by IWI followed by fast drying of the metal precursor/silica composite under air at 120 ± 1 °C for 24 h[5] and calcination under the above standard conditions. This reference NiO/SBA-15 sample was labeled as NC_0^{IWI}.

2.3. Physico-chemical Characterization. Inductively coupled plasma optical emission spectrometry (ICP-OES) was performed on a Perkin sequential scanning spectrometer to determine the elemental composition of catalysts (Ni, Cu, and Si). Before analysis, a known amount of calcined sample was introduced in a diluted HF-HCl solution and then digested under microwave.

Powder X-ray diffraction (XRD) was performed on a Bruker AXS D5005 X-ray diffractometer, using a CuKα radiation (λ = 1.54184 Å) as X-ray source. For small-angle analysis, the data were collected in reflection mode in the 2θ range from 0.75 to 5° with a step of 0.01° (step time of 10 s). For wide-angle analysis, the data were collected in the 2θ range from 10 to 80° with a step of 0.05° (step time of 8 s). Crystal phase identification was made by comparison with the ICDD database. The average crystallite size of NiO and CuO was calculated according to the Scherrer equation for the most intense diffraction lines at 2θ of 37.2 and 43.3°, and 35.5 and 38.7°, respectively.

Nitrogen physisorption was carried out on an Autosorb 1-MP automated gas sorption system (Quantachrome Instruments). Prior to analysis, the samples were outgassed under high vacuum at 350 °C for 3 h. The adsorption/desorption isotherms were obtained at −196 °C by allowing 4 min for equilibration between each successive point. Textural properties were determined from the isotherms by using the Autosorb 1 software, version 1.55. The BET surface area was determined using the multipoint algorithm. The *t*-plot method was applied to quantitatively determine the micropore volumes and to assess the micropore surface areas. To evaluate the metal oxide phase assembling mode inside the pores of mesostructured silica support, the normalized BET and micropore surface areas of catalysts were also calculated.[47] The mesopore size distribution was determined from the desorption branch of the isotherms using a nonlocal density functional theory (NL-DFT). The pore diameter of the primary mesopores was determined at the maximum differential pore volume registered in the pore size distribution profiles.

High-resolution transmission electronic microscopy (HRTEM) coupled with energy-dispersive X-ray spectroscopy (EDXS) was used to characterize the pore structure of SBA-15 support, distribution of NPs throughout the pores, the microstructure of NPs, as well as their chemical composition. The micrographs were obtained on a JEOL 2100 instrument (operated at 200 kV with a LaB_6 source and equipped with a Gatan Ultra scan camera). EDXS was carried out with a Hypernine (Premium) detector (active area: 30 mm^2) using the software SM-JED 2300T for data acquisition and treatment. EDXS analysis zone is defined on the particle, and is generally ranging from 5 to 15 nm. Before analysis, the sample was first included in a resin and then a cut of ~100 nm width was realized by ultramicrotomy.

Temperature-programmed reduction (TPR) runs were performed on a Autochem chemisorption analyzer from Micromeritics, equipped with TCD to monitor H_2 consumption and MS detector (Omnistar, Pfeiffer) to follow a possible desorption (H_2O, O_2, CO_2) from the catalyst surface or a possible leak (N_2). The calcined samples were introduced in a U-shape microreactor and activated under air flow (30 mL min^{-1}) at 500 °C for 1 h (heating ramp of 5 °C min^{-1}). After cooling to 50 °C, the 3 vol % H_2/Ar flow was stabilized (30 mL min^{-1}) and the TPR runs were then performed typically up to 900 °C (heating ramp of 5 °C min^{-1}).

In situ X-ray Photoelectron Spectroscopy (XPS) was performed before and after reduction of catalysts at 350 °C for 5 h (heating ramp of 5 °C min^{-1}) under 5 vol % H_2/He flow (30 mL min^{-1}). The spectra were acquired with a VG Escalab220XL spectrometer from Thermo. The analysis chamber was operated under ultrahigh vacuum of ~5 × 10^{-9} Torr. X-rays were produced by a magnesium anode working with Mg−Kα (1253.6 eV) radiation. For the measurements, the binding energy (BE) values were referred to the Si 2p photopeak at 103.8 eV. The surface Cu/Si, Ni/Si and Cu/M atomic ratios were calculated by correcting the corresponding peak intensities with theoretical sensitivity factors based on Scofield cross-sections.

In situ powder XRD patterns at wide angles were recorded on a Bruker D8 ADVANCE X-ray diffractometer equipped with a VANTEC-1 detector, using a CuKα radiation (λ = 1.54184 Å) as X-ray source. The calcined samples were first placed on a kanthal filament (FeCrAl) cavity and then subjected to thermoprogrammed reduction under a 3 vol % H_2/He flow (30 mL min^{-1}) from 30 to 550 °C (heating ramp of 5 °C min^{-1}). The in situ diffractograms were recorded at definite temperatures in the 2θ range from 15 to 70° with a step of 0.05° (step time of 2 s). Crystal phase identification was made by comparison with ICDD database.

Hydrogen chemisorption was performed on a volumetric Autosorb 1-MP (Quantachrome) apparatus. The calcined samples were first subjected to reduction at 350 °C for 10 h (heating ramp of 6 °C min^{-1}) under H_2 flow (1 L h^{-1}) and then outgassed under vacuum of ~10^{-4} Torr at the reduction temperature for 3 h. The first adsorption isotherms were obtained at 25 °C in the pressure range 120−240 Torr by allowing 30 min for equilibration prior to recording the first data point and 5 min between each successive point. The samples were then outgassed at the adsorption temperature for 30 min under vacuum of ~1 × 10^{-4} Torr and the readsorption isotherms were recorded. The extrapolation to zero pressure was taken as a measure of the hydrogen uptake on the metallic nickel phase. The uptake of irreversibly adsorbed hydrogen (V_{irr}) was calculated from the difference between the adsorption and readsorption isotherms and used as a measure of the number of surface Ni^0 atoms.

2.4. Evaluation of Catalytic Properties. The liquid phase hydrogenation of cinnamaldehyde was operated in a triphase system at atmospheric pressure, in a thermostatted three-neck glass reactor equipped with reflux condenser, hydrogen bubbler and magnetic stirrer. The following reaction conditions were applied: temperature of 150 °C, 1.05 g of trans-cinnamaldehyde, 25 mL of propylene carbonate, 0.265 g of catalyst, hydrogen flow of 1 L h^{-1} and stirring rate of 900 rpm. Prior to the catalytic runs, the calcined samples were gently crushed and sieved to obtain a granulometric fraction lower than 0.126 mm and then reduced to the metallic forms at 350 °C for

10 h (heating ramp of 6 °C min^{-1}) under H_2 flow (1 L h^{-1}). Preliminary tests made with different granulometric fractions and loadings of catalysts, and different stirring rates disclosed no diffusional limitations under the selected conditions. Aliquots of reaction mixture were withdrawn periodically and analyzed by GC (HP 5890 equipped with a DB-5 capillary column and a FID detector). The identification of the reaction products was achieved from the retention times of pure compounds and occasionally by GC-MS (Agilent 6890N system equipped with an Agilent 5973 MSD detector and a DB-5-ms column). The conversion of cinnamaldehyde and selectivity to the different hydrogenation products were calculated by taking into account the FID response factors for each compound.

3. RESULTS AND DISCUSSION

3.1. Structural Evolution and Textural Properties of NiO-CuO/SBA-15 Materials. The results of elemental analysis of the calcined metal oxide/SBA-15 samples (MO/SBA-15) are shown in Table 1. Results indicate similar total metal loadings of 5.85 ± 0.35 wt % and distinct Cu/M atomic ratios which range from 0 (NiO/SBA-15 sample: NC_0) to 1 (CuO/SBA-15 sample: NC_1), coherent with the progressive incorporation of more nickel-substituting copper atoms in the catalyst formulation.

Table 1. Chemical and Structural Properties of NiO-CuO/SBA-15 Materials

sample	Cu[a] (wt %)	Ni[a] (wt %)	Cu/M[a] ratio	d_{100}[b] (nm)	a_0[c] (nm)	crystal phase/d_{XRD}[d] (nm) NiO	CuO
SBA-15				9.1	10.5		
NC_0	0	5.6	0	8.3	9.5	9.2	
$NC_{0.2}$	1.2	4.5	0.20	8.8	10.2	8.7	n.d.[e]
$NC_{0.5}$	2.5	3.0	0.44	9.0	10.4	8.1	29.6
$NC_{0.8}$	5.1	1.1	0.81	9.1	10.5	14.5	29.5
NC_1	6.2	0	1	9.1	10.5		31.5

[a]Copper and nickel metal loading and Cu/M (M = Cu+Ni) atomic ratio by ICP-OES. [b]d_{100} is the lattice spacing obtained by low angle XRD. [c]a_0 is the hexagonal unit-cell parameter calculated using the equation: $a_0 = 2d_{100}/\sqrt{3}$. [d]Crystal phase identified by XRD at high angle; d_{XRD} is the average crystallite size evaluated with the Scherrer equation: $d_{hkl} = K(\lambda/\beta)\cos\theta$, where K is the structure constant (0.9 for spherical crystals), λ is the incident ray wavelength (0.1541 nm), β is the peak width at half height after correction for instrumental broadening (rad), and θ is the Bragg angle. [e]n.d. = not detected by XRD at high angle.

Figure 1 displays the XRD patterns in the small-angle domain for the parent SBA-15 and calcined monocomponent and bicomponent materials. The corresponding lattice spacings (d_{100}) and unit-cell parameters (a_0) are listed in Table 1. The XRD patterns show very intense diffraction peaks indexed to the (100) planes and two less intense peaks indexed to the (110) and (200) planes, which are characteristic to highly ordered hexagonal 2D structures of *p6mm* symmetry.[9] In addition, the presence of the (210) and (300) peaks indicates that the catalysts fully retain the long-range mesopore ordering and the excellent textural uniformity of the parent SBA-15, regardless of the Cu/M ratio. It can be also observed that the CuO/SBA-15 sample (NC_1) shows a very similar XRD pattern and identical cell parameter (a_0 of 10.5 nm) as its parent SBA-15, suggesting that the mesopores are essentially empty of oxide particles and that the majority of CuO crystallites are of low dispersion and located on the external surface as bulky aggregates.

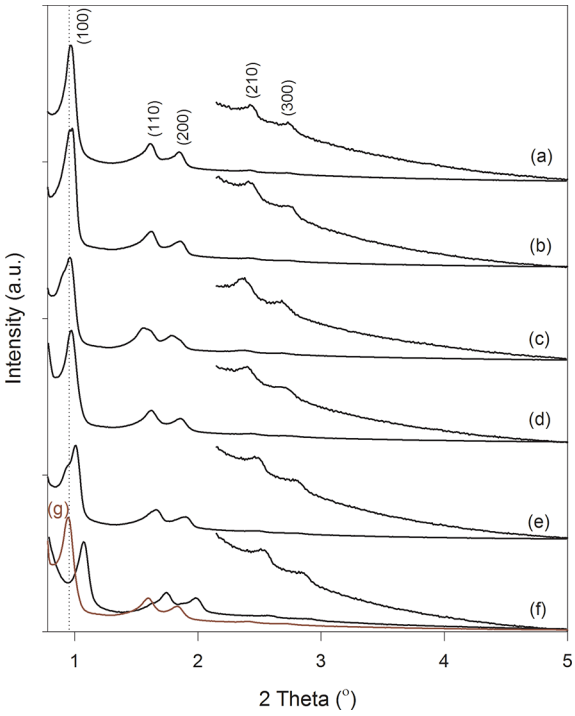

Figure 1. Low-angle XRD patterns between 0.75 and 5° for (a) parent SBA-15 and calcined (b) NC_1, (c) $NC_{0.8}$, (d) $NC_{0.5}$, (e) $NC_{0.2}$, (f) NC_0, and (g) NC_0^{IWI}.

At the other side, it is obvious that the NiO/SBA-15 sample (NC_0) shows a lower intensity of the (100) diffraction peak ($I_{(100)}$) and a smaller cell parameter (a_0 of 9.5 nm) as compared with the parent SBA-15, suggesting that the majority of NiO crystallites are highly dispersed and located within mesopores. The large discrepancy between the $I_{(100)}$ values obtained for the NC_1 and NC_0 samples can be readily explained by the scattering contrast between the SBA-15 silica walls and the material located inside mesopores.[48] Accordingly, when the SBA-15 mesopores are virtually empty (i.e., filled with air, the case of parent SBA-15 and NC_1), the scattering contrast is high and similar $I_{(100)}$ values are therefore obtained. However, when the SBA-15 mesopores are partially filled with a phase of comparable electron density to silica (i.e., filled with NiO, the case of NC_0), the scattering contrast diminished and $I_{(100)}$ of the MO/SBA-15 solid decreases correspondingly. As a general trend, it was observed that both $I_{(100)}$ and a_0 values increase with the gradual increase of the Cu/M ratio, indicating different dispersions of metal oxide crystallites and different assembling mode inside/outside the mesopores of SBA-15 host structure, which seem to significantly depend on the chemical composition of catalysts (vide infra). As concerns the reference NiO/SBA-15 sample (NC_0^{IWI}) obtained by IWI and drying at 120 °C, the corresponding XRD pattern (Figure 1g) shows a higher $I_{(100)}$ than that of NC_0 sample obtained by IWI-MD and the same peak positions as for the parent SBA-15, suggesting a lower degree of pore filling with oxide phases.

The textural properties of the calcined materials were investigated by nitrogen adsorption/desorption and the corresponding isotherms are shown in Figure 2 together with those of parent SBA-15. All MO-loaded SBA-15 samples exhibit isotherms of type IV with hysteresis loops of type H1, which

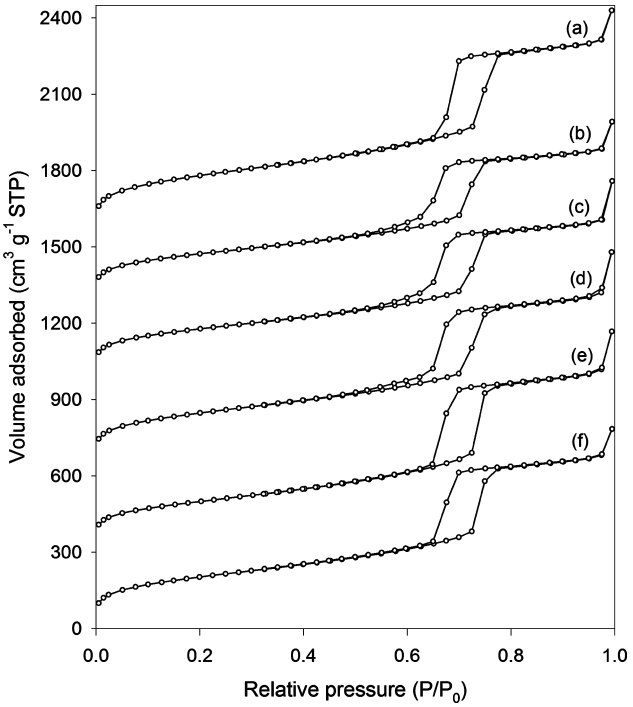

Figure 2. N_2 adsorption/desorption isotherms for (a) parent SBA-15, (b) NC_0, (c) $NC_{0.2}$, (d) $NC_{0.5}$, (e) $NC_{0.8}$, and (f) NC_1.

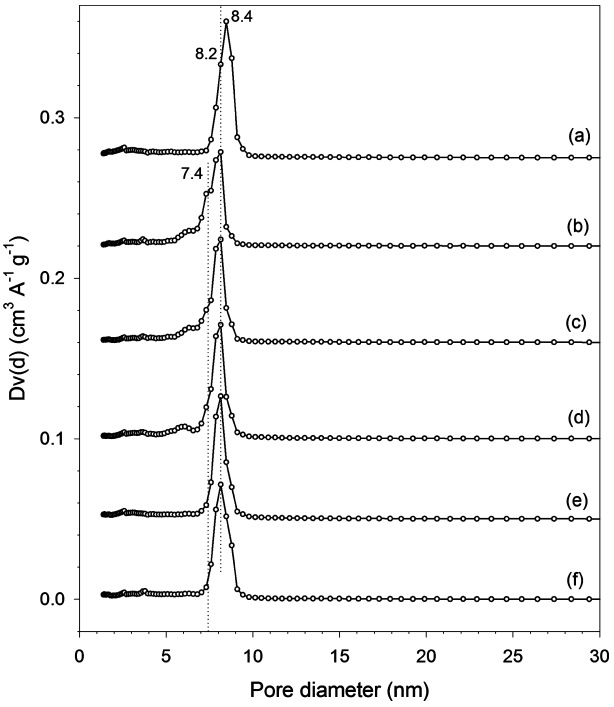

Figure 3. NL-DFT pore size distribution for (a) parent SBA-15, (b) NC_0, (c) $NC_{0.2}$, (d) $NC_{0.5}$, (e) $NC_{0.8}$, and (f) NC_1.

characterize the highly ordered mesoporous SBA-15 solids having a narrow pore size distribution of the cylindrical channels,[49] in good agreement with the results obtained by low-angle XRD. Likewise, it is noticed that the copper-rich $NC_{0.8}$ and NC_1 samples display isotherms very similar in shape with those of parent SBA-15 (isotherms e and f vs isotherm a), which are characterized by steep adsorption/desorption branches and uniform H1 hysteresis loops at relative pressures (P/P_0) of ~0.65−0.8, indicating that these catalysts essentially retain the initial texture of the parent SBA-15, as already suggested by low-angle XRD. In contrast, the samples with lower content of copper ($NC_{0.5}$, $NC_{0.2}$ and NC_0) show isotherms with less steep adsorption/desorption branches and capillary condensation steps shifted at lower relative pressures, when they are compared with the parent SBA-15 (isotherms d, c, and b, respectively, vs isotherm a). In addition, forced closures of the hysteresis loops are observed on the desorption branches at P/P_0 of ~0.5. These results indicate, on one hand, a decrease in the size of primary mesopores after MO loading, and on the other hand, a cavitation effect as a result of the partial blockage of primary mesopores and generation of ink-bottle type pores.[5,50] It appears that the magnitude of the cavitation effect increases with the amount of nickel in the catalyst formulation.

The pore size distribution curves shown in Figure 3 are in close agreement with the adsorption/desorption isotherms. Thus, the copper-rich samples display narrow NL-DFT pore size distributions with the maxima of the differential pore volume centered at 8.2 nm (curves e and f), slightly lower than the maximum at 8.4 nm registered for the parent SBA-15. In contrast, the samples with Cu/M ratios inferior to 0.5 exhibit a dual NL-DFT pore size distribution (curves b, c, and d), encompassing mesopores with average diameters of 8.2 and 7.4 nm, respectively. However, it was found that the relative distribution of these two types of mesopores depends on the Cu/M ratio, higher contents of nickel (the samples $NC_{0.2}$ and especially NC_0) resulting in increased contribution of the mesopores with the average pore diameter of 7.4 nm.

It is worth noting that by comparison with the nickel NC_0 sample obtained by IWI-MD, the sample NC_0^{IWI} shows isotherms which are very similar in shape with the parent SBA-15 and a monomodal pore size distribution with maximum at 8.2 nm (see Figure S2 in the Supporting Information), indicating that the catalyst mainly retains the initial texture of the parent host, in agreement with a low dispersion of the majority of NiO crystallites and their location on the external surface of SBA-15 as large aggregates, as already discussed in literature.[5,27]

On the basis of the adsorption/desorption isotherms, the textural properties of the SBA-15-supported oxides were calculated by specific algorithms and they are shown in Table 2. It can be observed that as compared with the parent SBA-15, depending on the chemical composition, the BET and microporous surface area of the MO/SBA-15 materials decrease from 803 and 183 $m^2\ g^{-1}$ to 617−717 and 104−142 $m^2\ g^{-1}$, respectively. In parallel, the total pore volume and micropore volume decrease from 1.12 and 0.082 $cm^3\ g^{-1}$ to 0.91−1.06 and 0.044−0.063 $cm^3\ g^{-1}$, respectively. However, the measured loss of surface area (e.g., 86−186 $m^2\ g^{-1}$ for the BET surface area) and pore volume (e.g., 0.06−0.21 $cm^3\ g^{-1}$ for the total pore volume) are much higher than the expected values because the effective volume occupied by the NiO and/or CuO is actually very small (i.e., 0.011−0.012 $cm^3\ g^{-1}$ as calculated from ICP-OES and by taking into account the density of MO). This discrepancy could be explained by pore blockage phenomena, which are known to result in some inaccessible porosity to the N_2 molecules, as reported for instance in the case of Co_3O_4 nanoparticles confined in the mesopores of SBA-15.[51,52] In order to scale the effect of Cu/M ratio in relation to these pore blockage phenomena, the

Table 2. Textural Properties of NiO-CuO/SBA-15 Materials

sample	S_{BET} [a] ($m^2\ g^{-1}$)	S_{micro} [b] ($m^2\ g^{-1}$)	V_{pore} [c] ($cm^3\ g^{-1}$)	V_{micro} [d] ($cm^3\ g^{-1}$)	D_p [e] (nm)
SBA-15	803	183	1.12	0.082	8.4
NC_0	617 (*0.83*)	104 (*0.61*)	0.91	0.044	7.4; 8.2
$NC_{0.2}$	633 (*0.85*)	110 (*0.65*)	0.94	0.047	7.4; 8.2
$NC_{0.5}$	672 (*0.90*)	129 (*0.76*)	1.01	0.057	7.4; 8.2
$NC_{0.8}$	722 (*0.98*)	145 (*0.86*)	1.09	0.066	8.2
NC_1	717 (*0.97*)	142 (*0.84*)	1.06	0.063	8.2

[a] S_{BET} is the total specific surface area obtained using the multipoint BET algorithm (P/P_0 = 0.1−0.25). [b] S_{micro} is the micropore surface area obtained by the *t*-method (de Boer statistical thickness = 0.38−0.65 nm); in brackets and italic are the normalized BET and microporous surface areas (NSA) calculated using the equation: NSA = $S_{catalyst}/(1 - x) \cdot S_{SBA\text{-}15}$, [47] where *x* is the weight fraction of the oxide phases estimated by elemental analysis, wt %. [c] V_{pore} is the total pore volume measured at P/P_0 = 0.97; [d] V_{micro} is the micropore volume obtained by the *t*-method; [e] D_p is the size of primary mesopores determined by the NL-DFT equilibrium algorithm for cylindrical pores.

normalized surface areas (NSAs) were calculated relative to the weight of the parent SBA-15 in the composite,[47] values around unity giving an indication of less pore blockage. As seen in Table 2, the Cu-rich samples NC_1 and $NC_{0.8}$ display BET NSAs of 0.97 and 0.98, respectively, showing no significant pore blockage because the mesopores are practically empty of MO crystallites, as also suggested by low angle XRD analysis. In contrast, the samples $NC_{0.5}$, $NC_{0.8}$ and NC_0 show BET NSAs smaller than unity (0.9, 0.85 and 0.83, respectively), indicating a partial pore blocking with confined MO particles.[5,53] On the other hand, the trend in the BET NSA variation suggests a less extent of mesopore blockage in the sample $NC_{0.5}$, probably due to a more homogeneous distribution of the NiO-CuO nanoparticles throughout the mesoporous support particles. However, it was interesting to find out that the microporous NSAs for $NC_{0.8}$ and NC_1 are of ∼0.85, far smaller than unity, suggesting that a population of CuO crystallites is occluded within/at the mouth of the SBA-15 micropores. With the further decrease in the Cu/M ratio, the microporous NSAs steadily fall up to 0.61, which suggests that the Ni sample contains the largest amount of such nanometric oxide crystallites. As described by Galarneau et al.,[15] when the hydrothermal synthesis is carried out at 100 °C (as in our case), SBA-15 displays a dual pore system composed of (i) primary mesopores with a pore diameter close to 8 nm and (ii) secondary micropores forming bridges between two adjacent primary mesopores and having variable diameters between 1.5 nm (supermicropores) and 4 nm (small mesopores). It is therefore likely that part of CuO and NiO has suffered the nucleation and growth inside/at the mouth of these microporous domains generating stable micropore-confined MO crystallites, whose fraction seems to depend on the chemical composition of catalysts.

XRD patterns recorded in the wide-angle domain for the calcined materials are depicted in Figure 4. According to the Cu/M ratios, the XRD patterns exhibit broad diffraction peaks characteristic to cubic NiO (ICDD 047−1049) as well as sharper diffraction peaks characteristic to monoclinic CuO (ICDD 048−1548), indicating that the NiO crystallite size is smaller than that of CuO. It was also found that the intensity of the XRD peaks follows the metal content incorporated in the catalyst formulation. The average sizes of metal oxide

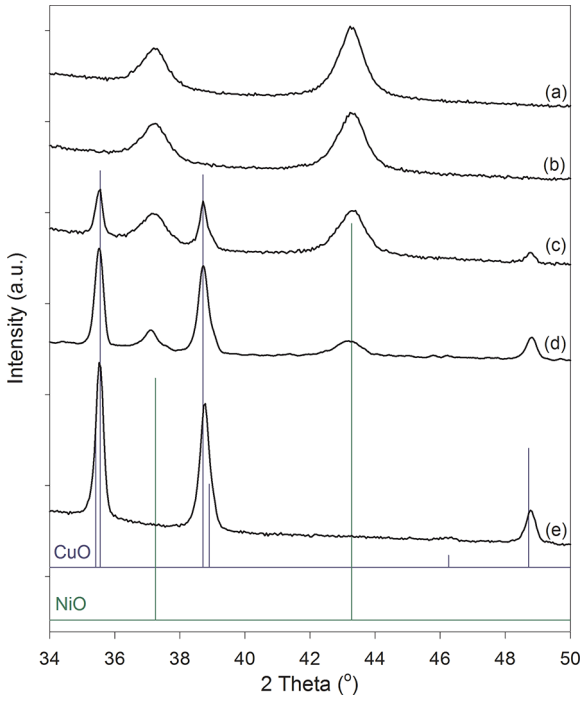

Figure 4. Enlarged view of the high-angle XRD patterns between 34 and 50° for (a) NC_0, (b) $NC_{0.2}$, (c) $NC_{0.5}$, (d) $NC_{0.8}$, and (e) NC_1.

crystallites (d_{NiO} and d_{CuO}) were estimated from the XRD peak broadenings and the results are shown in Table 1. For CuO, sizes between 29.5 and 31.5 nm were obtained, whereas for NiO, the crystallite sizes were between 8.1 and 14.5 nm, indicating that the dispersion of NiO is significantly higher than the dispersion of CuO. It can be observed that the progressive addition of Ni-substituting Cu atoms from zero up to a Cu/M ratio of ∼0.5 (samples NC_0, $NC_{0.2}$, and $NC_{0.5}$, patterns a−c) has a positive promoting effect on the NiO dispersion, d_{NiO} values decreasing from 9.2 to 8.7 and 8.1 nm, respectively. Interestingly, in this compositional range, d_{NiO} remains very close to the mesopore size of the parent SBA-15 (D_{pore} = 8.4 nm), because the NiO nanocrystallites are effectively confined and stabilized within the mesopores of SBA-15 and sintering resistant during air calcination.[29] However, it is disclosed that a further increase in the Cu/M ratio to 0.8 (pattern *d*) results in a reduced dispersion of both NiO (d_{NiO} = 14.5 nm) and CuO (d_{CuO} = 29.5 nm), respectively, indicating that at high concentration of copper, part of MO phase is transported outside the pores of SBA-15 during calcination, as already suggested by low-angle XRD and N_2 physisorption. Furthermore, it was surprising to observe that as far as the Cu/M ratio is close to 0.5 or higher, the CuO average crystallite size does not depend on the copper content in the catalyst formulation (d_{CuO} = 30.5 ± 1 nm). This apparent inconsistency was circumvented by considering the much broadened onsets and asymmetric shapes of the CuO diffraction peaks (patterns c, d, and e), which mean that a second population of small CuO crystallites must be present, as well. The same algorithm can be applied for the sample $NC_{0.8}$ (pattern d) which also displays a broadened onset of the NiO diffraction peak, pointing out a bimodal size distribution of the NiO crystallites. It may be concluded that d_{CuO} actually characterizes the first population of bulky CuO crystallites, which are most likely located on the external surface of SBA-15. These large CuO crystallites give rise to sharp reflections in the XRD patterns whose intensities

were observed to increase from $NC_{0.5}$ to NC_1 with the progressive increase in the Cu content. Nevertheless, it is worthy of note that when the Cu content is low (Cu/M ratio of ~0.2, pattern b), the reflections related to CuO are no longer detected, which might illustrate an effect of dilution of CuO crystallites into the NiO crystallites and the formation of a stable NiO−CuO solid solution.[34]

TEM analysis was further employed to study the morphology of nanoparticles as well as to provide local evidence on their distribution throughout the grains of mesoporous host. Some representative images are shown in Figure 5. As a first

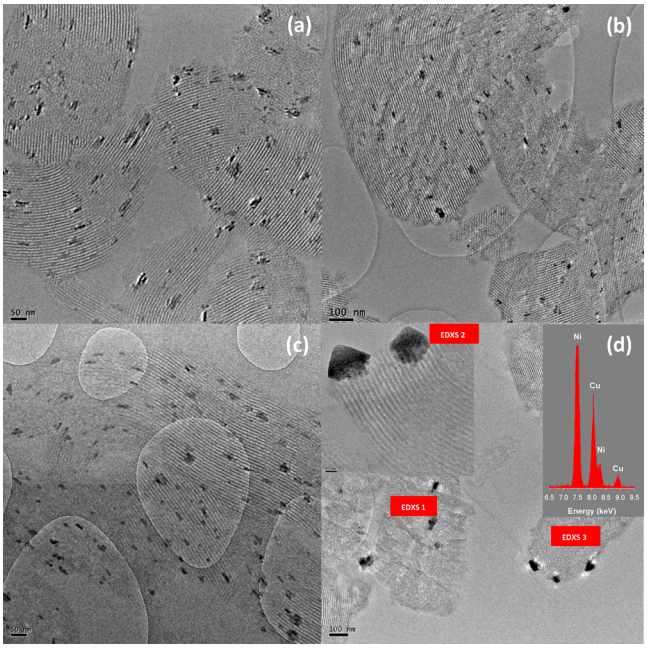

Figure 5. TEM images acquired along the [110] direction for (a) NC_0, (b) $NC_{0.2}$, (c) $NC_{0.5}$, and (d) $NC_{0.8}$. (Inset image d: EDX spectrum corresponding to the particles confined in mesopores, zone EDXS 1; the spectra corresponding to zones EDXS 2 and 3 are shown in the Supporting Information, Figures S3 and S4).

observation, all MO/SBA-15 solids exhibit typical highly ordered mesoporous SBA-15 structures composed of cylindrical mesochannels with a narrow size distribution. Figure 5a, b shows the TEM micrographs acquired for the NC_0 and $NC_{0.2}$ samples. No large aggregates on the external surface of silica grains were observed, reconfirming that the gentle drying of the metal precursor/silica impregnates is favorable to confine and stabilize the NiO and CuO particles within the mesopores of SBA-15 as well as to prevent the oxide phase transport at the external surface during calcination. Furthermore, the oxide nanoparticles appear well dispersed and uniformly distributed throughout the porous host grains under the form of rodlike particles with a diameter of ~8−9 nm (consistent with the pore diameter of the SBA-15 host) and variable lengths between ~10 and ~50 nm. Some nanorods have grown in adjacent mesopores forming nanobundle-like aggregates, more evidently for the NC_0 sample. Such particle morphology was previously observed for Co_3O_4 and MnO_2 nanowires obtained within SBA-15 mesopores by the "two solvent" method.[48,51,52] In contrast, the NiO/SBA-15 materials obtained by IWI were shown to contain both nanoparticles confined inside the pores and bulky phases outside the mesopores (20−60 nm particles),[27] in well agreement with our results of N_2 physisorption and TPR (vide infra) for the NC_0^{IWI} sample. As compared with the nickel-rich samples, a more evenly distribution of the individual particles inside the mesoporous silica matrix appeared for the sample $NC_{0.5}$ (Figure 5c). The particles show also rodlike morphologies with diameters of ~8−9 nm, yet they appear shorter (~10−40 nm) and with a lower degree of agglomeration as nanobundles. The more homogeneous distribution of MO nanoparticles in this Ni−Cu oxide sample may explain the lesser extent in pore blockage as compared, for instance, with the Ni sample. Likewise, no large MO aggregates were observed by TEM, though the presence of bulky CuO was advocated by XRD (Figure 4c). This means that such CuO aggregates are of rare occurrence. As illustrated in Figure 5d, when the Cu/M ratio was fixed at 0.8, part of the MO phase appeared as very large aggregates (size of ~100 nm) still stabilized at the mesopore mouths (inset Figure 5d), whereas the remaining part appeared confined within the mesopores as nanobundles. The heterogeneous distribution of particles clearly indicates that an excess of copper in the catalyst formulation has a negative effect on the dispersion of mixed oxides on SBA-15, in line with the bimodal size distribution of NiO and CuO crystallites suggested by XRD (Figure 4d). However, d_{NiO} and d_{CuO} for the sample $NC_{0.8}$ are much lower (14.5 and 29.5 nm, respectively) than the TEM size of bulky aggregates which indicates the polycrystalline nature of these aggregates. It is however interesting to observe by EDXS analyses that Cu and Ni are simultaneously present in both mesopore confined (zone EDXS 1, inset spectrum in Figure 5d; Cu/M ratio = 0.35) and aggregated particles (zone EDXS 2, Figure S3 in the Supporting Information; Cu/M ratio = 0.38), indicating on the one hand the existence of strong interactions between Ni and Cu and on the other hand the segregation of nickel at the surface of mixed oxide particles (bulk Cu/M = 0.81), irrespective of their size or crystallizing environment (i.e., confined in the pores or at the pore mouth). More interestingly, the EDX spectrum corresponding to the empty mesopores free of visible particles (zone EDXS 3, Figure S4 in the Supporting Information) shows a weak signal only for Cu atoms, indicating that a highly dispersed NiO-free CuO phase is also present, probably under the form of nanocrystallites occluded within/at the mouth of SBA-15 micropores, which was suggested before by N_2 physisorption. As for the nickel-free NC_1 sample, in the corresponding TEM images, only bulky CuO aggregates (size of ~70−100 nm) on the external surface were observed with no nanoparticles confined within the mesopores, whereas the EDXS spot analysis on the empty mesopores always suggests the presence of the highly dispersed CuO nanoparticles (a TEM image was selected for the graphical abstract).

As discussed above, the typical morphology of the MO nanoparticles confined within the mesochannels of mesoporous SBA-15 is rodlike with diameters close to the pore size of the support (~8−9 nm) and different lengths ranging from ~10 to ~50 nm. However, it was surprising to observe, for example, in the case of NC_0, that the lengths of the nanorods are much higher than the average size of the NiO crystallites (9.1 nm). To elucidate this point, the particle microstructure was further analyzed by HRTEM with increased contrast. Figure 6 shows some representative images acquired for the NiO/SBA-15 and the NiO−CuO/SBA-15 material with a Cu/M ratio of ~0.5. Observation along the [100] direction reveals first a structure of SBA-15 with the well-known hexagonal *p6mm* space group

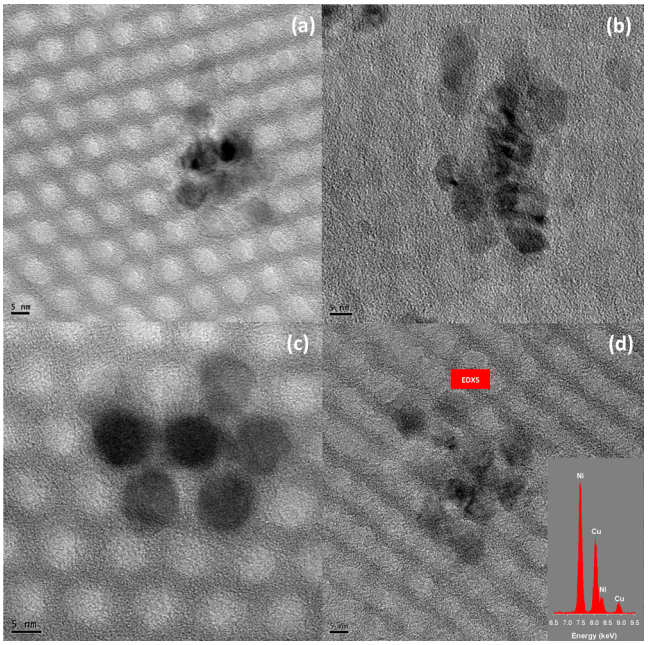

Figure 6. HRTEM images for (a, b) NC_0 and (c, d) $NC_{0.5}$ taken (a, c) along the [100] direction and (b, d) along the [110] direction. (Inset image d: EDX spectrum corresponding to the particles confined in mesopores).

symmetry. The pore diameter of the support is close to 8 nm in well agreement with the diameter of 8.4 nm determined by NL-DFT. For both compositions it can be observed that the MO nanorods have diameters which fit the pore size of the support. The nanorods grown in adjacent channels appear interconnected via micropores forming thus the nanobundle-like aggregates. Observation along the [110] direction discloses instead that the nanorod particles are actually of polycrystalline nature. They are composed of some elementary small oxide nanocrystals in contact with each other, more obviously for the NC_0 sample, and separated by grain boundaries, more obviously for the $NC_{0.5}$ sample. The lower degree of coarsening observed in the microstructure of NiO−CuO nanocrystals as compared with the microstructure of NiO may be associated with the effect of copper addition which decreases the average crystallite size of NiO (from 9.2 to 8.1 nm according to XRD). It is possible that the strong interactions between the Ni and Cu atoms as well as the formation of NiO−CuO solid solutions are responsible for this promoting effect of CuO addition on the dispersion of NiO particles.[30] This is in line with the simultaneous presence of copper and nickel in each aggregate (for example, the EDX spectrum shown in Figure 6d). It is interesting to mention that the EDXS Cu/M ratio was found to be lower (i.e., 0.3−0.35) than the bulk Cu/M ratio (i.e., 0.44), showing once again the tendency of nickel to enrich the surface of the mixed oxide particles, as already reported in recent literature.[31,37]

Overall, the catalyst composition was revealed to significantly influence the morphostructural and textural properties of SBA-15-supported NiO−CuO nanoparticles. As compared with the Ni material, the progressive increase of the Cu/M ratio has a positive effect on the dispersion of metal oxide particles, up to a value close to 0.5 (i.e., Cu/Ni ratio ∼1). Probably, in this compositional range there is an optimal interaction between Ni and Cu atoms which results in improved dispersion of both oxides in the mesoporous host structure and reduced pore blocking phenomena. The mixed oxides nanoparticles were uniformly distributed inside the mesoporous matrix as confined and stabilized polycrystalline nanorods. Nevertheless, the further increase in the Cu/M ratio has a negative effect on the stability and dispersion of metal oxide phases, which appear as bulky agglomerates close to the external surface of the host mesostructure besides the confined particles. This behavior may be related to the high mobility of copper precursors on the silica surface because of their weak interaction with the support.[6] However, by properly adjusting the chemical composition, the CuO nanoparticles can be stabilized through dilution in the NiO crystallites, which hinders their aggregation, as nicely illustrated with the composition $NC_{0.2}$.

3.2. Reducibility and Extent of Metal−Metal and Metal−Support Interactions in NiO−CuO/SBA-15 Materials. The reducibility of the calcined materials disclosed the existence of metal−metal and metal−support interactions in these solids. Figure 7 shows the TPR profiles of MO/SBA-15

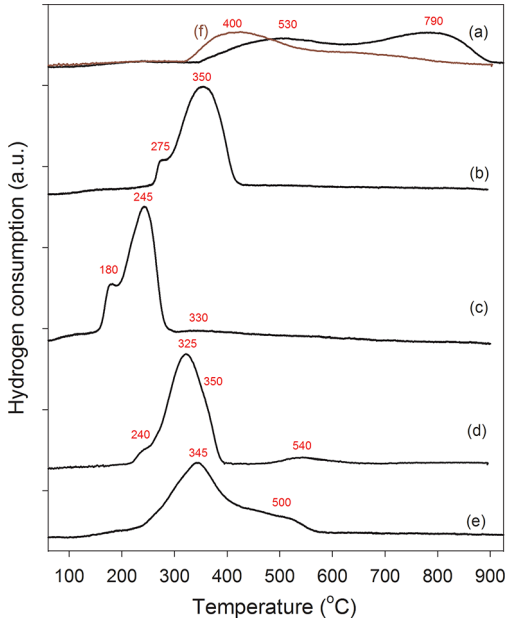

Figure 7. TPR profiles for (a) NC_0, (b) $NC_{0.2}$, (c) $NC_{0.5}$, (d) $NC_{0.8}$, (e) NC_1, and (f) NC_0^{IWI}.

catalysts with different chemical compositions as well as the TPR profile recorded for the NC_0^{IWI} sample obtained by conventional IWI. This reference sample shows a broad hydrogen consumption at ∼400 °C and a shoulder which vanishes at ∼900 °C (Figure 7f), attributed to the reduction of Ni^{2+} to Ni^0 from bulk NiO on the external surface of SBA-15 and in a weak interaction with the support (the major species) and NiO most probably confined within mesopores and in a strong interaction with the support (the minor species), respectively.[54] In contrast, NiO/SBA-15 sample obtained by IWI-MD (Figure 7a) presents a TPR profile composed of two broad reduction peaks with maxima at ∼530 and ∼790 °C, respectively. It is worthy of mention that the hardly reducible Ni species are generally characterized by strong interaction between supported nickel and silica support and are associated with highly dispersed nickel nanoparticles. Under these considerations, the lower extent of reducibility of NC_0 as compared with NC_0^{IWI} clearly indicates a better dispersion of the NiO nanoparticles as well as the lack of bulky NiO

aggregates, as already shown by various characterization techniques. In order to have some references which would allow ascribing the reduction peaks observed for NC_0, some examples from literature must be provided. Thus, the reduction of bulk NiO takes place at temperatures below 420 °C,[55] while NiO in strong interaction with alumina is reduced at 550−600 °C,[56] NiO from the decomposition of 1:1 nickel phyllosilicate (1:1 Ni PS) dispersed on SBA-15 by deposition−precipitation is reduced at ∼540 °C,[54] whereas nickel aluminate requires very high reduction temperatures, above 700 °C.[57] Therefore, it is most likely that the maximum at 530 °C is due to a NiO population in a strong interaction with silica. This is in agreement with our previous study,[29] which revealed that the main point of the IWI-MD method is to anchor and stabilize the NiO crystallites via layered 1:1 Ni PS phases located at the silica surface, in contrast to the IWI method where no stabilizing phases are involved. As the peak at ∼530 °C is reasonably described, the peak at ∼790 °C is yet to be explained, but intuitionally, it may correspond to the reduction of very stable and hardly reducible Ni^{2+} species. This can be rationalized by considering the N_2 physisorption data, which suggested that NiO/SBA-15 sample contains a large amount of nanometric crystallites. It is therefore postulated that the peak at 790 °C is due to the reduction of NiO nanocrystallites occluded in the microporous domains of SBA-15. It is noteworthy that such high reduction temperatures were observed before for the highly thermostable 2:1 nickel phyllosilicate phases,[58−60] but no connections are suspected yet with our results. At the other side, the CuO/SBA-15 sample (Figure 7e) is characterized by a main broad peak centered at ∼345 °C and a shoulder at ∼500 °C, both being associated to the reduction of Cu^{2+} to Cu^0. On the basis of the results presented so far, the primary peak may be attributed to the weakly dispersed bulky CuO aggregates located on the external surface of SBA-15, whereas the second peak is due to hardly reducible copper species such as copper silicate but most likely to CuO nanocrystallites confined in the micropores of SBA-15.[61−63] It is interesting to note that the reference CuO/SBA-15 sample prepared by IWI does not exhibit such a high-temperature reduction peak in the TPR profile, but only a reduction maximum close to 320 °C, typical to bulk CuO particles (not shown).

For the bicomponent $NC_{0.2}$ and $NC_{0.5}$ samples, the TPR profiles are shown in Figure 7b, c. The two main reduction maxima could be associated with the reduction of CuO and NiO, respectively, to the corresponding zerovalent metal particles. According to the literature, the reduction temperature of CuO depends on the particle size and dispersion, with lower reduction temperatures being associated with higher dispersions.[64−66] As compared with the monocomponent Ni and Cu samples, it is obvious that the addition of a small amount of Cu to Ni (Cu/M ratio of ∼0.2) has a significant effect in increasing the reducibility of NiO from ∼530 to ∼350 °C, and of CuO from ∼345 to ∼275 °C (Figure 7b).

With the increase in the Cu/M ratio to ∼0.5, the reduction maxima of CuO and NiO further shift to ∼180 and ∼245 °C, respectively, yet a broad feature at ∼330 °C could be still associated with the reduction of a minor bulky CuO phase suggested before by XRD (Figure 7c). This behavior illustrates, on one hand, the positive influence of NiO addition on the CuO dispersion by the dilution effect,[34,67] and on the other hand the synergistic effect between Ni and Cu.[34−38] Therefore, in a compositional range corresponding to Cu/M ratios of ∼0.2−0.5, the reducibility of both metal oxides is much improved as compared with their monocomponent counterparts due to the strong interaction between the two metals. The main reduction peaks may be actually associated with the reduction of the Cu and Ni cations in synergic interaction. The synergistic effect was shown to be at highest magnitude when the atomic ratio between Ni and Cu is close to 1. Indeed, as shown by EDXS, each particle/aggregate contains copper and nickel that demonstrates an intimate contact between the two metals and a strong interaction between them, which is confirmed herein by TPR analysis. The marked improvement in the reducibility of NiO NPs supported on SBA-15 materials could be also related to the ability of first generated copper nanoparticles to catalyze the reduction of less reducible Ni^{2+} metal cations by hydrogen spillover effect, which required a close contact between Cu and Ni in the same (nano)particle or aggregate.[30,35,41,68,69] Nonetheless, with the further increase in the Cu/M ratio at ∼0.8 (sample $NC_{0.8}$, Figure 7d), the TPR pattern displays different reduction peaks attributed to either CuO and NiO with behaviors close to the monocomponent counterparts (∼325 and ∼540 °C, respectively) or to CuO and NiO in synergic interaction (∼240 and ∼350 °C, respectively), indicating a heterogeneous distribution of the oxides in the support matrix, supporting thus the TEM analyses.

3.3. Surface Chemical States of NiO−CuO/SBA-15 Materials. XPS analysis was carried out to elucidate the surface chemical states of copper and nickel in the samples after calcination. Typically, the main Cu $2p_{3/2}$ photopeak of CuO is reported at ∼933.5 eV,[70] whereas for NiO the main Ni $2p_{3/2}$ peak is found at ∼854.9 eV.[71] XPS spectra are shown in the Supporting Information (Figures S5−S8), whereas the corresponding surface Cu/M as well as Cu/Si and Ni/Si atomic ratios are presented in Table 3 along with the binding energies (BE) for Cu $2p_{3/2}$ and Ni $2p_{3/2}$ obtained from curve-fitted values of experimental spectra. In all NiO−CuO/SBA-15 materials, irrespective of Cu/M ratio, surface copper exists in the oxidation state of Cu^{2+} (i.e., electron configuration d9), namely CuO in weak interaction with the silica support, as demonstrated by the Cu $2p_{3/2}$ peaks at 933.4−933.6 eV along with the presence in the XPS spectra of the satellite peaks due to electron shakeup.[72,73] The Ni $2p_{3/2}$ spectra in the Supporting Information, Figures S5−S8, exhibit the characteristic features of Ni^{2+} oxidation states with satellite peaks above the main photopeaks. The values of Ni $2p_{3/2}$ BE fall between 855.4 and 856.0 eV, indicating strong nickel-support interactions and suggesting that, in all calcined Ni-containing samples, surface nickel exists only as Ni^{2+} in 1:1 nickel phyllosilicate.[74,75] No

Table 3. XPS Results for the Calcined NiO/SBA-15 and NiO−CuO/SBA-15 Materials

sample	Cu $2p_{3/2}$ (eV)	Ni $2p_{3/2}$ (eV)	ΔE_{sat}[a] (eV)	Cu/Si[b]	Ni/Si[b]	Cu/M[b]
NC_0		855.6	6.1	0	0.023 *(0.061)*	0
$NC_{0.2}$	933.4	855.4	6.0	0.004 *(0.013)*	0.016 *(0.049)*	0.220 *(0.200)*
$NC_{0.5}$	933.6	856.0	5.9	0.007 *(0.022)*	0.012 *(0.029)*	0.375 *(0.436)*
$NC_{0.8}$	933.6	855.7	6.0	0.011 *(0.051)*	0.014 *(0.012)*	0.441 *(0.810)*

[a]Difference energy between Ni $2p_{3/2}$ main line and satellite line. [b]Surface atomic ratios and bulk atomic ratios (in parentheses).

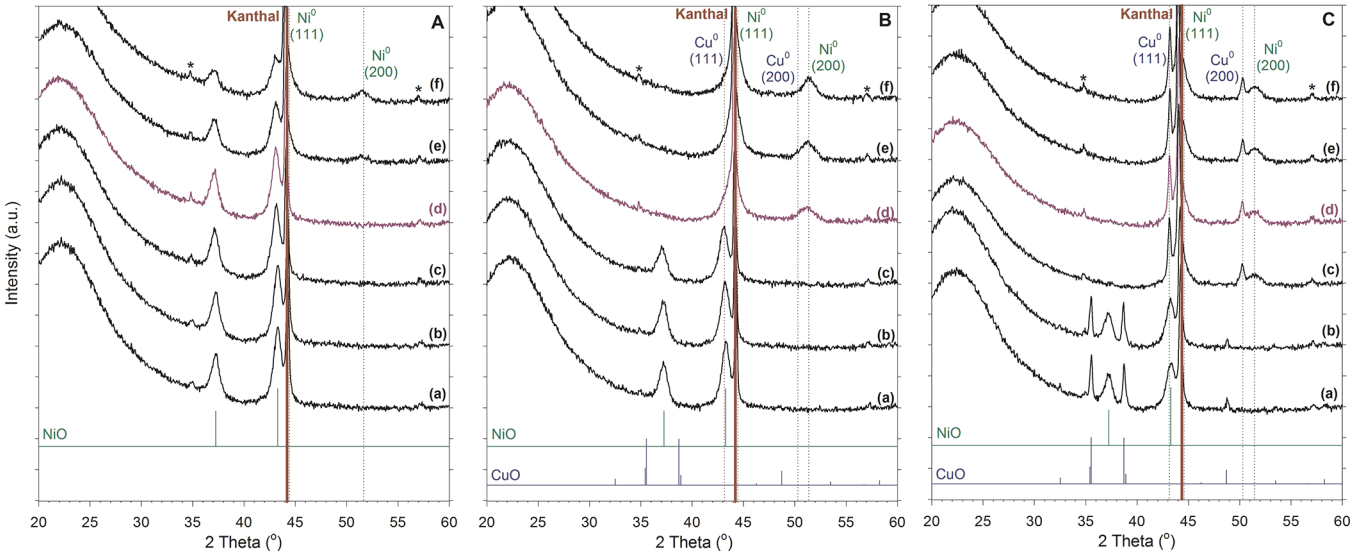

Figure 8. In situ XRD patterns for (A) NC_0, (B) $NC_{0.2}$, and (C) $NC_{0.5}$ after temperature-programmed reduction at (a) 30, (b) 150, (c) 250, (d) 350, (e) 450, and (f) 550 °C. * = 1:1 Ni PS.

contribution originating from surface NiO is evident, particularly due to satellite splittings ΔE_{sat} of ∼6 eV (Table 3), which are clearly not large enough for nickel oxide.[75] Therefore, the absence of NiO signatures in the XPS spectra indicates that the NiO−CuO particles observed in the TEM images are located within the mesopores of SBA-15 and of scarce occurrence at the surface to allow the detection of NiO by XPS. Indeed, the decrease in the Ni/Si (as well as Cu/Si) ratio from bulk to calcined catalysts indicates that a considerable amount of nickel (and copper) is present deep inside the SBA-15 mesopores as confined and stabilized particles and not deposited at the external surface of the support grain, in good agreement with the TEM results. Exception was noted for the $NC_{0.8}$ sample, which exhibits a higher Ni/Si surface ratio that in bulk as well as a lower Cu/M ratio, in line with the heterogeneous distribution of particles and their enrichment in nickel. In contrast, the samples $NC_{0.2}$ and $NC_{0.5}$ displayed Cu/M surface ratios close to the ratios in bulk (0.220 vs 0.200 and 0.375 vs 0.436, respectively), disclosing the homogeneous distribution of nickel and copper atoms throughout the host mesostructure.

3.4. Evolution of Crystal Phases of NiO−CuO/SBA-15 Materials during the Reduction under Hydrogen. The crystal phase evolution of Ni−Cu oxide nanoparticles during the thermoprogrammed reduction process was monitored by in situ XRD in the wide angle domain to further explore the structure and thermostability of evolved bimetallic nanoparticles. The recorded XRD patterns are shown in Figure 8. As a first observation, irrespective of the reduction temperature (T_R), XRD patterns show weak diffraction lines at 2θ of ∼35 and ∼57°, which are tentatively attributed to poorly crystallized phases of 1:1 Ni PS, exhibiting only two *hk* peaks (biperiodic structure) owing to the turbostratic stacking of the layers.[59,60] These minor phases were shown to be thermostable and not reducible after treatment under hydrogen at 550 °C (patterns f). After reduction at 30 °C (patterns a), the XRD diffractograms show the typical peaks of CuO phase (ICDD 048−1548) and of NiO phase (ICDD 047−1049). With the further increase in T_R, different crystal phase evolution was observed as a function of the chemical composition of catalysts.

Therefore, for the NiO/SBA-15 catalyst (Figure 8A), no significant changes are noticed in the XRD patterns until T_R = 450 °C (pattern e), when broad and weak diffraction peaks at 2θ of ∼44.5° (overlapping the diffraction line at 2θ of ∼44.5° due to the kanthal sample holder) and ∼51.5°, respectively, become discernible. These XRD peaks characterize the diffractions of (111) and (200) planes in metallic Ni^0 (ICDD 04−0850). In parallel, a decrease in the intensity of the NiO diffraction peaks was observed, indicating that the first population of NiO particles becomes to be reduced to metallic Ni at T_R between 350 and 450 °C. The intensity of the Ni^0 diffraction peaks slightly increases at T_R = 550 °C (pattern e) whereas the XRD peaks remain broad, indicating a high dispersion and high stability to sintering of the Ni^0/SBA-15 catalyst. These results are in excellent agreement with TPR, which indicated a first reduction maximum at ∼530 °C (Figure 6a). Furthermore, by combining in situ XRD with the TPR one can definitively associate the second reduction maximum at ∼790 °C with the reduction to Ni^0 of a population of NiO very stable and hardly reducible, namely NiO nanocrystallites occluded in the microporous domains of SBA-15.

For the $NC_{0.2}$ sample, the reduction of Cu and Ni oxides takes place at T_R between 250 and 350 °C (Figure 8B, patterns c and d), again in very well agreement with the corresponding TPR profile (Figure 6b). After T_R = 350 °C, only diffraction peaks typical to Ni^0 were observed, whereas the reduction to Cu^0 was suggested by the broad feature at 2θ of ∼43.2° (overlapping the kanthal diffraction line at 2θ of ∼44.5° and the XRD peak of NiO at 2θ of ∼43.3°) attributable to the diffraction of Cu^0 (111) plane (ICDD 04−0836). With the further increase in T_R to 450 and 550 °C (patterns e and f), the intensity of the Ni^0 diffraction peaks steadily increases but they remain broad, which indicates a high metal dispersion and high resistance to sintering of the $NC_{0.2}$ catalyst, as well.

In line with its TPR profile (Figure 6c), the sample $NC_{0.5}$ displays the highest extent of reducibility because the reduction of Cu and Ni oxides takes place at T_R between 150 and 250 °C (Figure 7C, patterns b and c). After T_R = 250 °C, beside the broad and weak diffraction peaks of Ni^0 (111) and (200), sharp reflections at 2θ of ∼43.2 and ∼50.2° ascribed to Cu^0 (111)

and (200) planes can be observed, as well. It is noteworthy that with the further increase in T_R up to 550 °C, no changes in the intensity or broadening of the XRD peaks of the metals are observed, indicating also for the $NC_{0.5}$ catalyst a high dispersion and high resistance to sintering under a hydrogen atmosphere.

3.5. NiO–CuO/SBA-15 Materials As Precursors for Highly Active Bimetallic Ni–Cu/SBA-15 Catalysts. On the basis of the TPR and in situ XRD analyses, a reduction temperature of 350 °C was considered appropriate to reduce the metal oxides to the metallic forms and to further study the surface chemical states of copper and nickel, the hydrogen chemisorption capacity and catalytic properties of bimetallic Ni–Cu/SBA-15 catalysts. To better illustrate the structure of Ni–Cu nanoparticles generated by the reduction of confined NiO–CuO nanoparticles, the in situ XRD patterns of the samples $NC_{0.2}$ and $NC_{0.5}$ after T_R = 350 °C (patterns *d* in Figure 8) were zoomed in the 2θ range of 40–55° and they are referred to the in situ XRD patterns of the monometallic counterparts in Figure 9. Albeit the (111) reflection of Ni

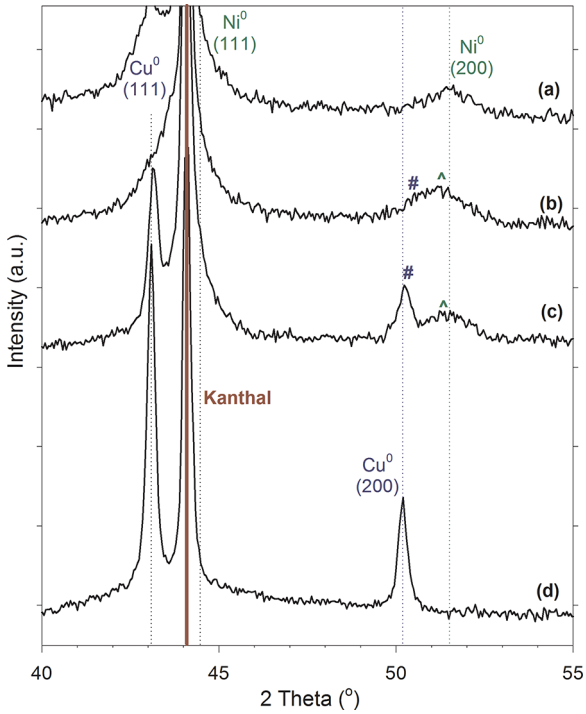

Figure 9. Enlarged view of the XRD patterns between 40 and 55° for the Ni–Cu/SBA-15 catalysts (a): NC_0^{R550}, (b) $NC_{0.2}$, (c) $NC_{0.5}$, and (d) NC_1. (NC_0^{R550} is the NC_0 reduced at 550 °C). # = Cu-rich phase; ^ = Ni-rich phase.

overlapped with the main reflection of the kanthal filament, the (200) reflections were intense enough to extract valuable information concerning the structure of bimetallic nanoparticles. Hence, two-peak overlapping patterns of these reflections can be clearly observed (patterns b and c), which disclose that in $NC_{0.2}$ and $NC_{0.5}$ samples, Ni–Cu nanoparticles supported on SBA-15 silica present two distinct metallic phases, i.e., Cu-rich phases and Ni-rich phases. Such phase segregation behavior was reported only for Ni–Cu NPs supported on alumina,[35,76] titania,[68] or ceria-lanthana,[36] thus for catalytic systems were strong metal–support interactions are involved. As shown in Figure 9, when the Cu/M ratio was decreased, the Ni^0 (200) peak position shifted to smaller 2θ angles, whereas the Cu^0 (200) peak position shifted to higher 2θ angles, along with the corresponding changes in the interplanar spacings and lattice parameters (see the Supporting Information, Table S1). This indicates the formation of alloys,[31,35] which is more evident for the sample $NC_{0.2}$. It is worthy of note that the (200) peaks associated to the Cu- and Ni-rich phases are broad and of low intensity, which suggests the high dispersion of the supported Cu-rich and Ni-rich metallic nanoparticles. It is obvious that the bimetallic Ni–Cu nanoparticles obtained herein do not present a complete solubility of Cu and Ni at reduction temperatures of 350 °C or above, probably due to the strong metal–support interactions that prevent the interdiffusion of Cu and Ni atoms.[36] The metal–support interaction may originate from the stabilization of Ni^0 at the surface of SBA-15 silica via the 1:1 nickel phyllosilicate phase combined with the confinement of precursor Ni–Cu NPs in mesopores and their geometrical stabilization in fixed positions along the ordered channels of SBA-15, as evidenced by complementary techniques such as XRD, nitrogen physisorption, TEM, and XPS spectroscopy.

Our results are extremely different from those obtained for Ni–Cu binary bulk alloys, which show continuous solid alloy solutions characterized by only one XRD reflection at 2$\theta \sim 52°$ associated to the (200) planes of both Cu^0 and Ni^0, respectively, in a wide range of Cu/M atomic ratios.[36] This was rationalized by considering that Ni and Cu have both fcc structures and similar lattice parameters of 3.51 and 3.61 Å, respectively. Furthermore, from thermodynamic considerations (i.e., lower surface free energy of Cu (1.85 J m^{-2}) as compared with Ni (2.45 J m^{-2})),[77] the segregation of Cu at the alloy surface is usually obtained.[78] However, it was reported by Li et al.[68] that when the structure of bimetallic Ni–Cu nanoparticles is kinetically controlled during the catalyst preparation, Cu-rich phases coexisting with Ni-rich phases can be rationally designed. They proposed the following mechanism, which can also explain the formation of our new Ni–Cu heterostructures: (i) the Cu precursor is reduced at lower temperatures than the Ni precursor; therefore, it is easier and quicker to form reduced Cu-containing species in the early stage of the reduction process, (ii) Cu and CuO have lower Tammann temperatures (i.e., 405 and 586 °C, respectively) than Ni and NiO (i.e., 590 and 841 °C, respectively); thus on the support surface, Cu species diffuse faster than Ni species leading to rapid formation of Cu crystals and (iii) the slower diffusion of the Ni species to the Cu nuclei leads to the formation of phase segregated Cu–Ni bimetallic particles.

The surface chemical states of copper and nickel in the reduced Ni–Cu/SBA-15 samples were further investigated by in situ XPS. The corresponding spectra are shown in the Supporting Information (Figures S5–S8) and the results are compiled in Table 4.

As compared with the calcined samples (Table 3), the Cu $2p_{3/2}$ binding energies of the reduced samples were shifted to lower values, whereas the satellite peaks disappeared due to the reduction of Cu^{2+} to Cu^0 and/or Cu^+.[69,71] Besides, with decreasing the copper content (increasing the nickel content), the Cu $2p_{3/2}$ BE shifted from 933.2 eV (sample $NC_{0.8}$) to lower values of 932.2 and 931.9 eV (samples $NC_{0.5}$ and $NC_{0.2}$, respectively). This seems to indicate that an electron transfer occurs between copper and nickel in the bimetallic Ni–Cu nanoparticles of $NC_{0.2}$ and $NC_{0.5}$ samples,[69] and support the idea of a strong interaction between the two metals. After reduction at 350 °C, the Ni $2p_{3/2}$ BE of Ni/SBA-15 slightly

Table 4. XPS Results for NiO/SBA-15 and NiO−CuO/SBA-15 Samples Reduced at 350 °C

	Cu $2p_{3/2}$ (eV)	Ni $2p_{3/2}$ (eV)				
sample	Cu^0	Ni^{2+}	Ni^0	Cu/Si[a]	Ni/Si[a]	Cu/M[a]
NC_0		855.3	n.d.[b]	0	0.020 *(0.061)*	0
$NC_{0.2}$	931.9	855.4	852.5	0.004 *(0.013)*	0.006 *(0.049)*	0.396 *(0.200)*
$NC_{0.5}$	932.2	855.9	852.7	0.004 *(0.022)*	0.006 *(0.029)*	0.394 *(0.436)*
$NC_{0.8}$	933.2	855.7	852.4	0.005 *(0.051)*	0.006 *(0.012)*	0.462 *(0.810)*

[a]Surface atomic ratios and bulk atomic ratios (in parentheses). [b]n.d.= not detected.

shifted to lower values (i.e., 0.3 eV), indicating that surface nickel remains as Ni^{2+} in 1:1 nickel phyllosilicate (BE = 855.3 eV). However, with the further increase in the copper content, new signatures of highly dispersed surface Ni^0 appeared in the XPS spectra (Ni $2p_{3/2}$ BE of 852.4−852.7 eV),[69,71] besides the characteristic features of Ni^{2+} in the reminiscent 1:1 Ni PS phases. These results are in very good agreement with TPR and in situ XRD results, and reconfirm that addition of copper is highly favorable in improving the reducibility of nickel cations. Also, the lower values of Ni/Si and Cu/Si ratios as compared with the bulk ratios indicates that nickel and copper remains located inside the SBA-15 mesopores after reduction, in line with the high resistance of Ni−Cu nanoparticles toward sintering, as demonstrated by other techniques. On the other hand, the evolution of surface Cu/M atomic ratios from the calcined to reduced samples indicates Cu segregation for $NC_{0.2}$, no significant Cu or Ni segregation for $NC_{0.5}$ and Ni segregation for $NC_{0.8}$, which may be due to compositional-dependent morphostructural and electronic properties of bimetallic Ni−Cu nanoparticles discussed above. However, it must be kept in mind that the XPS spectroscopy characterizes only the chemical composition in the near-surface region and therefore does not provide information on the composition of bimetallic Ni−Cu nanoparticles located within the mesopores of SBA-15. To circumvent this drawback, complementary characterization was made by hydrogen chemisorption.

The chemisorption of hydrogen at 25 °C was performed over the Ni−Cu/SBA-15 catalysts reduced at 350 °C. It is necessary to point out that copper does not have the capacity to dissociatively chemisorb H_2 molecules at this low temperature due to its completely filled d10 electronic configuration,[42,43,79] and therefore the hydrogen uptake provides information only about the nickel surface composition. The effect of Cu/M ratio on the uptake of irreversibly adsorbed hydrogen (V_{irr}) is shown in Figure 10. It can be first observed that the increase in the Cu/M ratio to ∼0.2 leads to a marked increase in the hydrogen uptake as compared with the Ni catalyst (V_{irr} of 108.7 and 59.3 μmol g^{-1}, respectively).

In agreement with the TPR and in situ XRD and XPS analyses, this behavior may be mainly related to the improved reducibility of $NC_{0.2}$ sample which brings about an enhanced number of surface Ni^0 metal atoms. On the other hand, when the Ni surface composition of bimetallic catalysts is investigated relative to the nickel-free NC_1 sample, it can be observed that hydrogen uptake decreases almost linearly with the increase in the Cu/M ratio up to a small value corresponding to the monometallic Cu catalyst. The trend of the hydrogen

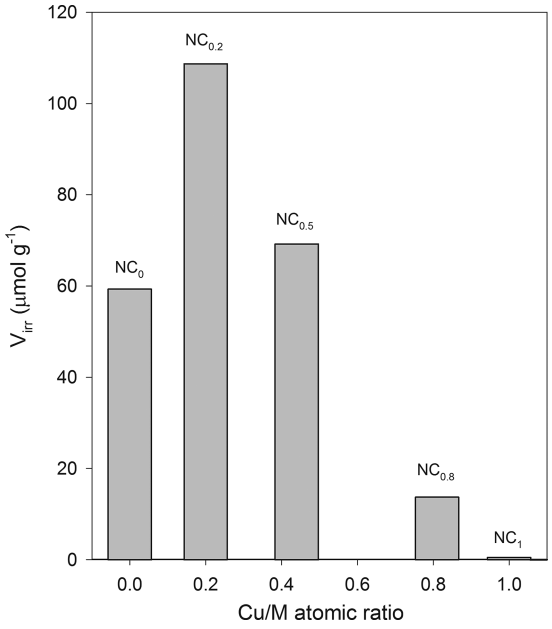

Figure 10. Hydrogen chemisorption capacity of bimetallic Ni−Cu/SBA-15 catalysts reduced at 350 °C.

chemisorption capacity with the chemical composition of catalysts clearly shows that no significant segregation of copper (i.e., no dilution of the nickel surface sites) takes place at the surface of Ni−Cu nanoparticles, as long as the samples with Cu/M ratio up to 0.5 are analyzed. Likewise, it suggests that the SBA-15-supported Ni−Cu bimetallic catalysts do not have intermetallic or homogeneous alloyed structures but they are rather heterostructures in which the two bimetallic nanoparticles (i.e., the Cu-rich and Ni-rich phases) can share a mixed interface. Different from heterostructures, the Ni−Cu alloy structures display significant copper surface segregation even at a very low content of copper in the catalyst formulation (i.e., Cu/M atomic ratio of 0.05), which results in the dilution of most surface nickel atoms and in a severe decline in their hydrogen chemisorption capacity.[80]

The catalytic performance of Ni−Cu/SBA-15 materials was evaluated in the liquid-phase hydrogenation of cinnamaldehyde (CNA) as benchmark reaction. It proceeds via pathways that first involve hydrogenation of C═C and C═O double bonds of CNA molecules to hydrocinnamaldehyde (HCNA) and cinnamyl alcohol (CNOL), respectively, followed by total hydrogenation of these primary products to hydrocinnamyl alcohol (HCNOL) (Scheme 1).

In the Supporting Information, Figure S9 shows the evolution of CNA conversion with the reaction time for the tested catalysts, whereas Figure S10 displays the products distribution profiles. The catalytic activities expressed as total conversion of CNA after 180 min of reaction are presented in Table 5 together with the measured selectivity levels. It can be first observed that the monometallic NC_0 catalyst exhibits a much higher activity than the homologous catalyst prepared by IWI (86.1 vs 57.2%), which is readily explained by taking into account the better dispersion of nickel and stronger metal−support interactions achieved by the IWI-MD method. In addition, NC_0 catalyst displays a very high and stable selectivity to HCNA (∼94%) even at conversion levels as high as ∼95% (see Figure S10 A in the Supporting Information), demonstrating a high performance in the hydrogenation of C═C double.

Scheme 1. Reaction Pathways for the Hydrogenation of Cinnamaldehyde

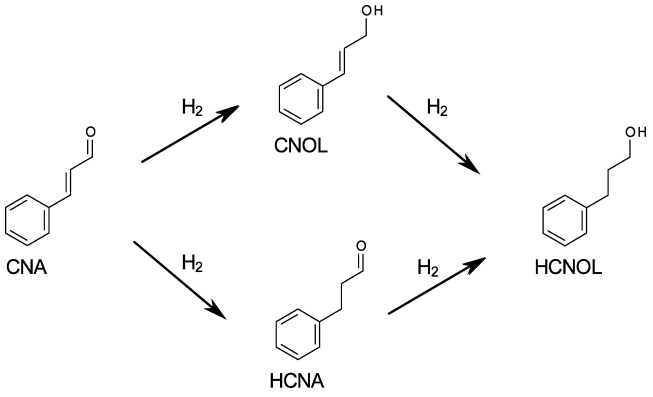

Table 5. Catalytic Properties of Ni−Cu/SBA-15 in the Hydrogenation of Cinnamaldehyde

		selectivity[b]		
sample	conversion[a] (mol %)	S_{HCNA} (mol %)	S_{CNOL} (mol %)	S_{HCNOL} (mol %)
NC_0 [IWI]	57.2	94.2	1.6	4.2
NC_0	86.1	94.0	1.4	4.6
$NC_{0.2}$	99.3	90.8	5.4	3.8
$NC_{0.5}$	72.0	88.4	7.2	4.4
$NC_{0.8}$	11.5	83.9	9.7	6.4
NC_1	1.1			

[a]Total conversion of CNA measured after 180 min of reaction. [b]Selectivity levels were measured at a CNA iso-conversion of ∼20 mol %.

This result can be related to the low d-bandwidth of metallic nickel (3.0 eV), which is known to hinder the adsorption of α,β-unsaturated aldehydes via the C═O bond.[41,81] In contrast, the copper sample showed a negligible catalytic activity (1.1%) due to the low capacity of poorly dispersed copper to activate the hydrogen molecules (see Figure 10). Indeed, examples from literature show that in order to have enhanced chemisorption capacity and hence superior intrinsic activity in the hydrogenation of CNA, the electronic density of supported Cu^0 species must be high, which can be achieved only for highly dispersed copper nanoparticles.[82−84] As compared with the monometallic Ni catalyst, the bimetallic $NC_{0.2}$ catalyst showed higher activity (99.3%). As a general trend, the gradual increase in the Cu/M ratio in bimetallic catalysts is followed by a decrease in the activity, which was consistent with the hydrogen chemisorption capacity of Ni−Cu/SBA-15 materials (see the Supporting Information, Figure S11). The enhanced performance of bimetallic $NC_{0.2}$ catalysts can be therefore explained by the synergistic effects between nickel and copper, as discussed before. Among other effects, the addition of inert copper to active Ni can modify the adsorption mode of CNA molecules on the catalyst surface through electronic effects. This may explain the moderate decrease in the selectivity to HCNA from ∼94 to ∼84% (and the increase in the selectivity to CNOL from ∼1.5 to ∼10%) with the gradual increase in the Cu/M atomic ratio (Table 5).

However, analysis of our data by comparison with the results from literature is quite difficult, particularly due to the different reaction conditions (e.g., temperature, pressure, and polarity of the solvent). In addition, the hydrogenation of α,β-unsaturated aldehydes is known as a reaction very sensitive to the molecular structure of the substrate. For instance, the branching in the vicinity of the C═C bond favors the formation of the unsaturated alcohol (UOL). This may explain why UOL is selectively obtained from cinnamaldehyde in comparison with acrolein. The catalytic performance also depends on the nature of metals because of their different geometric and electronic properties, which influence not only surface reactions but also the adsorption modes of substrates, the latter being key to activate the C═C and/or C═O bond of the α,β-unsaturated aldehydes. For instance, the non-noble metals such as Ni and Co generally display lower intrinsic activity as compared with noble metals such as Ru Pt, Pd, etc. Hence, in the hydrogenation of C═C bonds from olefins, the following order of activity was obtained: Rh > Ru > Pd > Pt > Ni > Co ≫ Cu,[85] which is very similar to the trend observed in the hydrogenation of α,β-unsaturated aldehydes.[45] To compensate this difference in activity and for economic reasons, the catalyst loading is usually 0.05−0.5% for noble metals, and 5−15% for other metals.[85] On the other hand, with increasing metal loading, the activity of the hydrogenation catalysts usually reaches a limiting value. For example, in a preliminary optimization study, we investigated the effect of total metal loading (i.e., 1, 2, 5, and 10 wt %) for Ni−Cu/SBA-15 catalysts obtained by IWI-MD (Cu/M atomic ratio of 0.5) and observed that the activity in the hydrogenation of CNA increases with the loading up to 5 wt % and then slightly increases for 10 wt %. Likewise, the catalytic performance must be analyzed in relation to the chemical and morphostructural properties of metallic active sites (e.g., electronic density, surface chemical composition, particle size and shape).[45] Particularly for the supported bimetallic Ni−Cu catalysts, it was reported that the nature of support and the surface structure including bimetallic composition, the binding energy, and the bonding morphologies play a crucial role in the selective hydrogenation of α,β-unsaturated aldehydes. For these reasons, the catalytic results reported in literature for this bimetallic system are somewhat controversial. For instance, it was reported for the Ni−Cu/Al_2O_3 catalysts prepared by coprecipitation that the increase in the Cu/Ni ratio enhances the selectivity to UOL in the hydrogenation of crotonaldehyde.[86] The effect of copper was interpreted in terms of the different strength of electron-pair donor and electron-pair acceptor of hydrogen bonded on nickel and on copper. In the hydrogenation of citral over Ni−Cu/KL zeolite, the most active catalysts corresponded to a Cu/(Cu +Ni) atomic ratio of ∼0.2, whereas the selectivity toward UOL decreased with the content of copper. This was explained by the formation of Ni−Cu alloys partially covered with segregated copper.[41] Similar results were obtained in the hydrogenation of citral over Ni−Cu/graphite.[40] The intrinsic activity of catalysts and the UOL selectivity slightly increased as compared with Ni/graphite. However, when the hydrogenation of cinnamaldehyde was performed over the same catalysts, it was observed that the activity does not significantly change with the increase in the copper content, whereas the selectivity to the UOL slightly increases. These results were interpreted on the basis of the dominant hydrogenating character of nickel. Hydrogenation of citral was also performed over Ni−Cu/SiO_2.[39] It was reported that the bimetallic catalyst with Cu/(Cu +Ni) of ∼0.2 shows a much improved catalytic activity than Ni/SiO_2. This was rationalized by electronic effects (i.e., electron transfer from copper to nickel) resulting in enhanced electron density of Ni in bimetallics. Nevertheless, the

selectivity of Ni−Cu/SiO_2 to UOL was not considerably improved as compared with the monometallic nickel catalyst (79 vs 74%).

In the light of these results from literature, the composition-dependent catalytic performance of bimetallic Ni−Cu/SBA-15 demonstrated herein supports the formation of new Ni−Cu heterostructures with particular geometric and/or electronic properties. However, the intrinsic mechanism underlying these properties still requires further investigations. It is finally worthy of note that the evolution of the catalytic performance of Ni−Cu/SBA-15 with the Cu/(Cu+Ni) ratio is very similar to that recently reported for Pd−Au/MSN (MSN = mesoporous silica nanoparticles).[24] Such a comparison is particularly interesting by taking into account that (i) Ni and Pd, and Cu and Au belong to the same groups in the periodic table of elements (i.e., VIIIB and IB, respectively), (ii) synergistic effects between Ni and Cu, and Pd and Au were demonstrated in both cases, particularly geometric and electronic effects and (iii) Ni−Cu and Pd−Au are highly dispersed and confined within the mesopores of ordered mesoporous silicas. Thus, for both catalytic systems, enhanced chemisorption capacity and catalytic activity were noted for the samples with Cu/(Cu+Ni) and Au/(Au+Pd) atomic ratio of ∼0.2, but most interesting, the chemoselective properties were practically identical (∼85% HCNA at complete conversion of CNA). It can be therefore concluded that by controlling the interaction between the two metal components, it is possible to fine-tune the geometric and electronic properties of the bimetallic nanoparticles and rationally design performance catalysts for the selective hydrogenation of α,β-unsaturated aldehydes.

4. CONCLUSIONS

The incipient wetness impregnation followed by mild drying (IWI-MD approach) was employed to obtain confined NiO and NiO−CuO nanoparticles, which are stabilized within the pores of micro/mesoporous SBA-15 by Ni-support (via nickel phyllosilicate phases) and Cu−Ni interactions. It was demonstrated that the catalyst composition has a significant effect on the morphostructural and textural properties of SBA-15-supported NiO−CuO nanoparticles. Thus, as compared with the monometallic Ni material, the progressive increase of the Cu/M ratio has a positive effect on the dispersion of metal oxide particles as well as their reducibility, up to a value close to 0.5, which was explained by strong interactions between Ni and Cu atoms in the same nanoparticles. Nevertheless, the further increase in the Cu/M ratio negatively influences the stability and dispersion of metal oxide phases, which appear heterogeneously distributed on the SBA-15 support as both bulky agglomerates and confined particles, respectively. This behavior was associated with the insufficient stabilization by Cu−Ni interactions and weak Cu−support interactions. Because of their controllable properties, the SBA-15-confined polycrystalline NiO−CuO nanoparticles with properly adjusted chemical composition can be successfully used as precursors to generate bimetallic Ni−Cu/SBA-15 catalysts with greatly improved reducibility and hydrogen chemisorption capacity as well as enhanced catalytic performance.

More detailed investigations are currently underway on the application of IWI-MD method to obtain highly thermostable and dispersed monocomponent and bicomponent metal (oxide) nanoparticles based on Cu, Ni, and Co supported on mesoporous SBA-15 with the focus put on other key factors which affect their morphostructural properties (e.g., metal loading and the atomic ratio between the two metal components, drying time and temperature, and pretreatment conditions during the calcination and reduction steps).

■ ASSOCIATED CONTENT

Ⓢ Supporting Information

FESEM images of SBA-15 support; N_2 adsorption/desorption isotherms for NiO/SBA-15 obtained by IWI; EDX spectra; XPS spectra; XRD analysis of bimetallic samples; conversion of CNA vs reaction time; product distribution profiles; Correlation between the catalytic activity and hydrogen chemisorption capacity. This material is available free of charge via the Internet at http://pubs.acs.org.

■ AUTHOR INFORMATION

Corresponding Author

*E-mail: aungureanu@tuiasi.ro (A.U.); sebastien.royer@univ-poitiers.fr (S.R.). Tel: +40-232 278683 (A.U.); +33-(0)5-4945-3479 (S.R.).

Author Contributions

The manuscript was written through contributions of all authors. All authors have given approval to the final version of the manuscript.

Notes

The authors declare no competing financial interest.

■ ACKNOWLEDGMENTS

This work was partially supported by a grant of the Romanian National Authority for Scientific Research, CNCS−UEFISCDI, Project PN-II-ID-PCE-2011-3-0868. B.D. acknowledges the project PERFORM-ERA "Postdoctoral Performance for Integration in the European Research Area" (ID-57649), financed by the European Social Fund and the Romanian Government. Dr. S. Casale (Université Pierre et Marie Curie, Paris) is acknowledged for the FESEM analyses.

■ REFERENCES

(1) Campelo, J. M.; Luna, D.; Luque, R.; Marinas, J. M.; Romero, A. A. *ChemSusChem* **2009**, *2*, 18−45.
(2) Jiang, H. L.; Xu, Q. *J. Mater. Chem.* **2011**, *21*, 13705−13725.
(3) Cuenya, B. R. *Thin Solid Films* **2010**, *518*, 3127−3150.
(4) Greeley, J.; Mavrikakis, J. *Nat. Mater.* **2004**, *3*, 810−815.
(5) Sietsma, J. R. A.; Meeldijk, J. D.; Versluijs-Helder, M.; Broersma, A.; van Dillen, A. J.; de Jongh, P. E.; de Jong, K. P. *Chem. Mater.* **2008**, *20*, 2921−2931.
(6) Munnik, P.; Wolters, M.; Gabrielsson, A.; Pollington, S. D.; Headdock, G.; Bitter, J. H.; de Jongh, P. E.; de Jong, K. P. *J. Phys. Chem. C* **2011**, *115*, 14698−14706.
(7) Duprez, D.; Demicheli, M.; Marecot, P.; Barbier, J.; Feretti, O. A.; Ponzi, E. N. *J. Catal.* **1990**, *124*, 324−335.
(8) Kresge, C. T.; Leonowicz, M. E.; Roth, W. J.; Vartuli, J. C.; Beck, J. S. *Nature* **1992**, *359*, 710−712.
(9) Zhao, D. Y.; Feng, J. L.; Huo, Q. S.; Melosh, N.; Fredrickson, G. H.; Chmelka, B. F.; Stucky, G. D. *Science* **1998**, *279*, 548−552.
(10) Moller, K.; Bein, T. *Chem. Mater.* **1998**, *10*, 2950−2963.
(11) Shi, J. L.; Hua, Z. L.; Zhang, L. X. *J. Mater. Chem.* **2004**, *14*, 795−806.
(12) Lu, A. H.; Schüth, F. *Adv. Mater.* **2006**, *18*, 1793−1805.
(13) Sun, J.; Bao, X. *Chem.—Eur. J.* **2008**, *14*, 7478−7488.
(14) Cassiers, K.; Linssen, T.; Mathieu, M.; Benjelloun, M.; Schrijnemakers, K.; van der Voort, P.; Cool, P.; Vansant, E. F. *Chem. Mater.* **2002**, *14*, 2317−2324.
(15) Galarneau, A.; Cambon, H.; Di Renzo, F.; Ryoo, R.; Choi, M.; Fajula, F. *New J. Chem.* **2003**, *27*, 73−79.

(16) Yang, C. M.; Lin, H. A.; Zibrowius, B.; Spliethoff, B.; Schüth, F.; Liou, S. C.; Chu, M. W.; Chen, C. H. *Chem. Mater.* **2007**, *19*, 3205−3211.
(17) Valange, S.; Palacio, R.; Charmot, A.; Barrault, J.; Louati, A.; Gabelica, Z. *J. Mol. Catal. A: Chem.* **2009**, *305*, 24−33.
(18) Zhong, X.; Barbier, J., Jr.; Duprez, D.; Zhang, H.; Royer, S. *Appl. Catal., B* **2012**, *121*, 123−134.
(19) Yuranov, I.; Moeckli, P.; Suvorova, E.; Buffat, P.; Kiwi-Minsker, L.; Renken, A. *J. Mol. Catal. A: Chem.* **2003**, *192*, 239−251.
(20) Yang, C. M.; Liu, P. H.; Ho, Y.; Chiu, C.; Chao, K. *Chem. Mater.* **2003**, *15*, 275−280.
(21) Sun, J.; Ma, D.; Zhang, H.; Liu, X.; Han, X.; Bao, X.; Weinberg, G.; Pfänder, N.; Su, D. *J. Am. Chem. Soc.* **2006**, *128*, 15756−15764.
(22) Lee, B.; Ma, Z.; Zhang, Z.; Park, C.; Dai, S. *Microporous Mesoporous Mater.* **2009**, *122*, 160−167.
(23) Liu, X.; Wang, A.; Wang, X.; Mou, C. Y.; Zhang, T. *Chem. Commun.* **2008**, 3187−3189.
(24) Yang, X.; Chen, D.; Liao, S.; Song, H.; Li, Y.; Fu, Z.; Su, Y. *J. Catal.* **2012**, *291*, 36−43.
(25) Yamamoto, K.; Sunagawa, Y.; Takahashi, H.; Muramatsu, A. *Chem. Commun.* **2005**, 348−350.
(26) Garcia-Cuello, V. S.; Giraldo, L.; Moreno-Piraj, J. C. *J. Chem. Eng. Data* **2011**, *56*, 1167−1173.
(27) Wolters, M.; van Grotel, L. J. W.; Eggenhuisen, T. M.; Sietsma, J. R. A.; de Jong, K. P.; de Jongh, P. E. *Cat. Today* **2011**, *163*, 27−32.
(28) Sietsma, J. R. A.; Meeldijk, J. D.; den Breejen, J. P.; Versluijs-Helder, M.; van Dillen, A. J.; de Jongh, P. E.; de Jong, K. P. *Angew. Chem., Int. Ed.* **2007**, *46*, 4547−4549.
(29) Ungureanu, A.; Dragoi, B.; Chirieac, A.; Royer, S.; Duprez, D.; Dumitriu, E. *J. Mater. Chem.* **2011**, *21*, 12529−12541.
(30) Carrero, A.; Calles, J. A.; Vizcaíno, A. J. *Appl. Catal., A* **2007**, *327*, 82−94.
(31) Chen, L. C.; Lin, S. D. *Appl. Catal., B* **2011**, *106*, 639−649.
(32) Chuang, K. H.; Liu, Z. S.; Chang, Y. H.; Lu, C. Y.; Wey, M. Y. *Reac. Kinet. Mech. Cat.* **2010**, *99*, 409−420.
(33) Studt, F.; Abild-Pedersen, F.; Wu, Q.; Jensen, A. D.; Teme, B.; Grunwaldt, J.-D.; Norskov, J. K. *J. Catal.* **2012**, *393*, 51−60.
(34) Habimana, F.; Li, X.; Ji, S.; Lang, B.; Sun, D.; Li, C. *J. Nat. Gas Chem.* **2009**, *18*, 392−398.
(35) De Rogatis, L.; Montini, T.; Cognigni, A.; Olivi, L.; Fornasiero, P. *Cat. Today* **2009**, *145*, 176−185.
(36) Lin, J. H.; Biswas, P.; Guliants, V. V.; Misture, S. *Appl. Catal., A* **2010**, *387*, 87−94.
(37) Gandarias, L.; Requies, J.; Arias, P. L.; Armbruster, U.; Martin, A. *J. Catal.* **2012**, *290*, 79−89.
(38) Boudjahem, A. G.; Bouderbala, W.; Bettahar, M. *Fuel Process. Technol.* **2011**, *92*, 500−506.
(39) Mäki-Arvela, P.; Tiainen, L. P.; Lindblad, M.; Demirkan, K.; Kumar, N.; Sjöholm, R.; Ollonqvist, T.; Väyrynen, J.; Salmi, T.; Murzin, D. Y. *Appl. Catal., A* **2003**, *241*, 271−288.
(40) Asedegbega-Nieto, E.; Bachiller-Baeza, B.; Guerrero-Ruiz, A.; Rodríguez-Ramos, I. *Appl. Catal., A* **2006**, *300*, 120−129.
(41) Álvarez-Rodríguez, J.; Cerro-Alarcón, M.; Guerrero-Ruiz, A.; Rodríguez-Ramos, I.; Arcoya, A. *Appl. Catal., A* **2008**, *348*, 241−250.
(42) Dalmon, J. A.; Martin, G. A. *J. Catal.* **1980**, *66*, 214−221.
(43) Martin, G. A.; Dalmon, J. A. *J. Catal.* **1982**, *75*, 233−242.
(44) Gallezot, P.; Richard, D. *Catal. Rev.−-Sci. Eng.* **1998**, *40*, 81−126.
(45) Mäki-Arvela, P.; Hájek, J.; Salmi, T.; Murzin, D. Yu. *Appl. Catal., A* **2005**, *292*, 1−49.
(46) Sun, X.; Shi, Y.; Zhang, P.; Zheng, C.; Zheng, X.; Zhang, F.; Zhang, Y.; Guan, N.; Zhao, D.; Stucky, G. D. *J. Am. Chem. Soc.* **2011**, *133*, 14542−14545.
(47) Vradman, L.; Landau, M. V.; Kantorovich, D.; Koltypin, Y.; Gedanken, A. *Microporous Mesoporous Mater.* **2005**, *79*, 307−318.
(48) Impéror-Clerc, M.; Bazin, D.; Appay, M. D.; Beaunier, P.; Davidson, A. *Chem. Mater.* **2004**, *16*, 1813−1821.
(49) Kruk, M.; Jaroniec, M. *Chem. Mater.* **2001**, *13*, 3169−3183.
(50) Van Der Voort, P.; Ravikovitch, P. I.; De Jong, K. P.; Neimark, A. V.; Janssen, A. H.; Benjelloun, M.; Van Bavel, E.; Cool, P.; Weckhuysen, B. M.; Vansant, E. F. *Chem.Commun.* **2002**, 1010−1011.
(51) Van der Meer, Y. J.; Bardez, I.; Bart, F.; Albouy, P. A.; Wallez, G.; Davidson, A. *Microporous Mesoporous Mater.* **2009**, *118*, 183−188.
(52) Taghavimoghaddam, J.; Knowles, G. P.; Chaffee, A. L. *J. Mol. Catal. A: Chem.* **2012**, *358*, 79−88.
(53) Sietsma, J. R. A.; Friedrich, H.; Broersma, A.; Versluijs-Helder, M.; van Dillen, A. J.; de Jongh, P. E.; de Jong, K. P. *J. Catal.* **2008**, *260*, 227−235.
(54) Liu, H.; Wang, H.; Shen, J.; Sun, Y.; Liu, Z. *Appl. Catal., A* **2008**, *337*, 138−147.
(55) Brown, R.; Cooper, M. E.; Whan, D. A. *Appl. Catal.* **1982**, *3*, 177−186.
(56) Guimon, C.; Auroux, A.; Romero, E.; Monzon, A. *Appl. Catal., A* **2003**, *251*, 199−214.
(57) Choudary, V. R.; Rajput, A. M. *J. Catal.* **1993**, *139*, 326−328.
(58) Burattin, P.; Che, M.; Louis, C. *J. Phys. Chem. B* **1999**, *103*, 6171−6178.
(59) Sivaiah, M. V.; Petit, S.; Barrault, J.; Batiot-Dupeyrat, C.; Valange, S. *Cat. Today* **2010**, *157*, 397−403.
(60) Sivaiah, M. V.; Petit, S.; Beaufort, M. F.; Eyidi, D.; Barrault, J.; Batiot-Dupeyrat, C.; Valange, S. *Microporous Mesoporous Mater.* **2011**, *140*, 69−80.
(61) Owens, L.; Tillotson, T. M.; Hair, L. M. *J. Non-Cryst. Solids* **1995**, *186*, 177−183.
(62) Tkachenko, O. P.; Klementiev, K. V.; van den Berg, M. W. E.; Gies, H.; Grünert, W. *Phys. Chem. Chem. Phys.* **2006**, *8*, 1539−1549.
(63) Tkachenko, O. P.; Klementiev, K. V.; Koc, N.; Yu, X.; Bandyopadhyay, M.; Grabowski, S.; Gies, H.; Grünert, W. *Stud. Surf. Sci. Catal.* **2004**, *154*, 1670−1678.
(64) Tu, C. H.; Wang, A. Q.; Zheng, M. Y.; Wang, X. D.; Zhang, T. *Appl. Catal., A* **2006**, *297*, 40−47.
(65) Zheng, X. C.; Wu, S. H.; Wang, S. P.; Wang, S. R.; Zhang, S. M.; Huang, W. P. *Appl. Catal., A* **2005**, *283*, 217−223.
(66) Liu, Z.; Amiridis, M. D.; Chen, Y. *J. Phys. Chem. B* **2005**, *109*, 1251−1255.
(67) El-Shobaky, H. G. *Appl. Catal., A* **2004**, *278*, 1−9.
(68) Li, P.; Liu, J.; Nag, N.; Crozier, P. A. *J. Catal.* **2009**, *262*, 73−82.
(69) Yin, A.; Wen, C.; Guo, X.; Dai, W. L.; Fan, K. *J. Catal.* **2011**, *280*, 77−88.
(70) Gervasini, A.; Manzoli, M.; Martra, G.; Ponti, A.; Ravasio, N.; Sordelli, L.; Zaccheria, F. *J. Phys. Chem. B* **2006**, *110*, 7851−7861.
(71) Naghash, A. R.; Etsell, T. H.; Xu, S. *Chem. Mater.* **2006**, *18*, 2480−2488.
(72) Kirumakki, S. R.; Shpeizer, B. G.; Sagar, G. V.; Chary, K. V. R.; Clearfield, A. *J. Catal.* **2006**, *242*, 319−331.
(73) Huang, Z.; Cui, F.; Kang, H.; Chen, J.; Zhang, X.; Xia, C. *Chem. Mater.* **2008**, *20*, 5090−5099.
(74) Vedrine, J. C.; Hollinger, G.; Duc, T. M. *J. Phys. Chem.* **1978**, *82*, 1515−1520.
(75) Lehmann, T.; Wolff, T.; Hamel, C.; Veit, P.; Garke, B.; Seidel-Morgenstern, A. *Microporous Mesoporous Mater.* **2012**, *151*, 113−125.
(76) Lee, J. H.; Lee, E. G.; Joo, O. S.; Jung, K. D. *Appl. Catal., A* **2004**, *269*, 1−6.
(77) Van Stiphout, P. C. M.; Stobbe, D. E.; Scheur, F. Th. V. D.; Geus, J. W. *Appl. Catal.* **1988**, *40*, 219−246.
(78) Sinfelt, J. H. *Acc. Chem. Soc.* **1977**, *10*, 15−20.
(79) Kacimi, S.; Duprez, D.; Dalmon, J. A. *J. Chem. Phys.* **1997**, *94*, 535−552.
(80) Sinfelt, J. H.; Carter, J. L.; Yates, D. J. C. *J. Catal.* **1972**, *24*, 283−296.
(81) Singh, U. K.; Vannice, M. A. *J. Catal.* **2001**, *199*, 73−84.
(82) Marchi, A. J.; Gordo, D. A.; Trasarti, A. F.; Apesteguıa, C. R. *Appl. Catal., A* **2003**, *249*, 53−67.
(83) Valange, S.; Derouault, A.; Barrault, J.; Gabelica, Z. *J. Mol. Catal. A: Chem.* **2005**, *228*, 255−266.
(84) Liu, Z.; Yuan, Y.; Mi, J.; Tan, X.; Song, Y. *Catal. Commun.* **2012**, *21*, 58−62.

(85) Hagen, J. *Industrial Catalysis: A Practical Approach*; Wiley-VCH: Weinheim, Germany, 2006.
(86) Noller, H.; Lin, W. N. *J. Catal.* **1984**, *85*, 25−30.